Impact of the Asian Monsoon Anticyclone on the Variability of mid-to-upper tropospheric methane above the Mediterranean Basin

P. Ricaud[1], B. Sič[1], L. El Amraoui[1], J.-L. Attié[1,2], R. Zbinden[1], P. Huszar[3], S. Szopa[4], J. Parmentier[1], N. Jaidan[1], M. Michou[1], R. Abida[1], F. Carminati[1,2,5], D. Hauglustaine[4,6], T. August[7], J. Warner[5], R. Imasu[8], N. Saitoh[9] and V.-H. Peuch[10]

[1]CNRM-GAME, Météo-France/CNRS UMR 3589, Toulouse, France

[2]Université de Toulouse, Laboratoire d'Aérologie, CNRS UMR 5560, Toulouse, France

[3]Department of Meteorology and Environment Protection, Faculty of Mathematics and Physics, Charles University, Prague, V Holešovičkách 2, Prague 8, 18000, Czech Republic

[4]Laboratoire des Sciences du Climat et de l'Environnement, CNRS UMR 1572, Gif sur Yvette, France

[5]University of Maryland, College Park, Maryland, USA

[6]Laboratoire Image Ville Environnement, CNRS UMR 7362, Strasbourg, France

[7]EUMETSAT, Darmstadt, Germany

[8]University of Tokyo, Tokyo, Japan

[9]Center for Environmental Remote Sensing, Chiba University, Japan

[10]European Centre for Medium-Range Weather Forecasts, Reading, UK

Correspondence to: P. Ricaud (philippe.ricaud@meteo.fr)

In revision, *Atmospheric Chemistry and Physics Discussions*

Version 16, 16 September 2014

Abstract

The space and time variabilities of methane (CH_4) total column and upper tropospheric mixing ratios are analyzed above the Mediterranean Basin (MB) as part of the Chemical and Aerosol Mediterranean Experiment (ChArMEx) programme. Since the analysis of the mid-to-upper tropospheric CH_4 distribution from spaceborne sensors and model outputs is challenging, we have adopted a climatological approach and have used a wide variety of datasets. We have combined spaceborne measurements from the Thermal And Near infrared Sensor for carbon Observations-Fourier Transform Spectrometer (TANSO-FTS) instrument on the Greenhouse gases Observing SATellite (GOSAT) satellite, the Atmospheric InfraRed Spectrometer (AIRS) on the AURA platform and the Infrared Atmospheric Sounder Interferometer (IASI) instrument aboard the MetOp-A platform with model results from the Chemical Transport Model (CTM) MOCAGE, and the Chemical Climate Models (CCMs) CNRM-AOCCM and LMDz-OR-INCA (according to different emission scenarios). In order to minimize systematic errors in the spaceborne measurements, we have only considered maritime pixels over the MB. The period of interest spans from 2008 to 2011 considering satellite and MOCAGE data and, regarding the CCMs, from 2001 to 2010. Although CH_4 is a long-lived tracer with lifetime of ~12 years and is supposed to be well mixed in the troposphere, an East-West gradient in CH_4 is observed and modelled in the mid-to-upper troposphere with a maximum in the Western MB in all seasons except in summer when CH_4 accumulates above the Eastern MB. The peak-to-peak amplitude of the East–West seasonal variation in CH_4 above the MB in the upper troposphere (300 hPa) is weak but almost twice greater in the satellite measurements (~25 ppbv) than in the model data (~15 ppbv). The maximum of CH_4 in summer above the Eastern MB can be explained by a series of dynamical processes only occurring in summer. The Asian monsoon traps and uplifts high amounts of CH_4 to the upper troposphere where they build up. The Asian Monsoon Anticyclone redistributes these elevated CH_4 amounts towards North Africa and Middle East to finally reach and descent in the Eastern MB. In

the lower troposphere, the CH_4 variability is mainly driven by the local sources of emission in the vicinity of the MB.

1. Introduction

During the last decades, the impact and the role that atmospheric trace gases play in climate and air pollution changes have been the source of major concerns. In Intergovernmental Panel on Climate Change (IPCC, 2007), the ongoing changes of our atmosphere (composition, climate, air pollution, radiation) are reported. Among trace gases, methane (CH_4), carbon dioxide (CO_2), and nitrous oxide (N_2O) are predominant constituents which play an important role in atmospheric changes because they are strongly influenced by human activities. In the frame of predicting the future of the Earth's climate (IPCC, 2007), knowledge of today's CO_2, CH_4 and N_2O sources and sinks, spatial distribution and time variability is essential and this study will be dedicated to CH_4.

The net positive radiative impact of the human activity on climate, starting from 1750, has been evaluated to 1.6 [+0.6 to +2.4] Wm^{-2} (IPCC, 2007). In the atmosphere, these long-lived greenhouse gases, e.g., CH_4, N_2O and CO_2, account for 2.63 ± 0.26 Wm^{-2} and are the predominant radiative terms. CO_2, with tropospheric lifetime of 30–95 years, has a radiative efficiency of 1.4×10^{-5} $Wm^{-2}ppb^{-1}$, but CH_4 and N_2O, with tropospheric lifetimes of 12 and 114 years, respectively, are intensely more efficient by 3.7×10^{-4} and 3.03×10^{-3} $Wm^{-2}ppb^{-1}$, respectively. IPCC (2007) estimated CH_4 and N_2O to be responsible of 0.48 [+0.43 to 0.53] and 0.16 [+0.14 to 0.18] Wm^{-2}, respectively in the radiative forcing changes.

The Mediterranean Basin (MB) is located in a transitional zone between subtropical and mid-latitudes regimes (Lionello, 2012), highly sensitive to climate change. To illustrate, global (or regional) model simulations tend to show a pronounced decrease in precipitation (2000-2100), especially in the warm season (Giorgi and Lionello, 2008), and Lionello (2012) reported on an observed summer West-East asymmetry in precipitation over the MB (1979-2002). In terms of anthropogenic pollution sources, the MB is at the confluence of three continents, Europe, Africa and Asia. The impact of these distinct continental sources such as from manufactures and densely populated coastal areas (e.g. Marseille, Barcelona, Athens, Tunis, Cairo, Genoa or Roma) (Kanakidou et al, 2011; Im and Kanakidou, 2012) or forest fires (e.g. South East of France, Corsica,

Portugal, Greece) (Cristofanelli et al., 2013) is still not perfectly understood, especially on the O_3 and CO budgets in which CH_4 interplays through complex reactions with nitrogen oxides (NOx) (Dentener et al., 2005). Besides these regional sources, polluted air masses may originate from Asia during the summer monsoon period (Randel and Park, 2006), Africa through the Hadley cell and upper level anticyclone (Ziv et al., 2004; Liu et al., 2009) and North America through the westerlies (Christoudias et al, 2012). The Expérience sur Site pour Contraindre les Modèles de Pollution atmosphérique et de Transport d'Emission (ESCOMPTE) campaign (June-July 2001) aimed to characterize the summer time pollution events in the vicinity of Marseille, France (Cros et al., 2004). The goal of the Mediterranean Intensive Oxidant Study (MINOS) campaign (July-August 2001) in the eastern Mediterranean was to measure long-range transport of air pollution and aerosols from South East Asia and Europe towards the MB (Ladstätter-Weißenmayer et al.,, 2003; Scheeren et al., 2003). They have demonstrated the importance of coastal and synoptic transport mechanisms on the variability of constituents but were not adapted to assess the budgets of O_3, CO and long-lived species.

The ChArMEx (Chemistry and Aerosol Mediterranean Experiment) Project (http://charmex.lsce.ipsl.fr/) is the atmospheric chemistry component of a large multidisciplinary Mediterranean regional program proposed and conducted by France. It intends, among other objectives, to quantify processes explaining the temporal evolution of chemical compounds and aerosols in the troposphere above the Mediterranean Basin (MB). To achieve these goals over the first phase (2010-2015), the program uses data from satellites, ground-based, sondes, aircraft, models and assimilation in order to evaluate 1) the variabilities and recent trends of several species (e.g. O_3, CO, N_2O) and aerosols, 2) the synoptic-scale circulation that controls their transport, and 3) the future chemical climate over the MB by 2100.

The past/present nadir-viewing instruments able to actually measure CH_4 in the troposphere have been/are:

1) the Interferometric Monitor for Greenhouse gases (IMG) instrument operating in the Thermal Infrared (TIR) aboard the ADvanced Earth Observing Satellite (ADEOS-1) platform in 1996-1997 (Clerbaux et al., 1998);

2) the near-IR (NIR) Scanning Imaging Absorption Spectrometer for Atmospheric Chartography (SCIAMACHY) aboard the ENVIronment SATellite (ENVISAT) platform (Buchwitz et al., 2000) from 2002 to 2012;

3) the Tropospheric Emission Spectrometer (TES) operating in the TIR aboard the Aura platform (Worden et al., 2012) from 2004 to date;

4) the Thermal And Near infrared Sensor for carbon Observations – Fourier Transform Spectrometer (TANSO-FTS) on the Greenhouse gases Observing SATellite (GOSAT) platform (Yokota et al., 2009) both in the Short-Wave InfraRed (SWIR) and in the TIR from 2008 to date;

5) the Atmospheric InfraRed Sounder (AIRS) aboard the Aqua platform (Xiong et al., 2008) measuring in the TIR from 2004 to date;

6) the Infrared Atmospheric Sounding Interferometer (IASI) instrument aboard the MetOp-A and -B platforms (Hilton et al., 2012) operating in the TIR from 2008 to date, and aboard the MetOp-C platform expected to be launched in 2016.

Table 1 synthesizes the above mentioned information and shows the nadir-viewing instrument capability to measure tropospheric CH_4. The sensitivity of the TIR to measure CH_4 is rather weak except on areas showing a high thermal contrast at the surface (vertical gradient of temperature between the surface and the lowermost planetary boundary layer) as the ones encountered over the tropics (Crevoisier et al., 2013) contrarily to the measurements performed in the SWIR (Yoshida et al., 2013). In the NIR, analyses are essentially restricted to areas over land because the retrievals over sea are considered less reliable due to fairly low surface albedo of water, which results in low signals and thus in low signal-to-noise ratios (Georgoulias et al., 2011).

In parallel to the satellite data, models have also been used in order to assess the variability, sources and sinks, and future trends of the long-lived species. Examples are: CH_4 emission and flux

128 estimates at global scales (Bergamaschi et al., 2009; Bousquet et al., 2011), future evolution of
129 long-lived species included in the international Atmospheric Chemistry and Climate Model
130 Intercomparison Project (ACCMIP) involving more than 10 different models (Lamarque et al.,
131 2013).

132 Numerous studies have examined the variabilities of atmospheric compounds above the MB to
133 highlight the processes (sources and sinks) associated by coupling surface, balloon-borne, airborne,
134 spaceborne measurements with models results at different scales, from mesoscales to global scales.
135 Constituents are for instance aerosols (Nabat et al., 2012), radionuclides (Masson et al., 2010),
136 ozone (Liu et al., 2009), carbon monoxide (Drori et al., 2012). From these references, we note the
137 impact of 1) the different meteorological regimes and 2) the seasonal variabilities of the emissions
138 of atmospheric constituents, e.g. CO emitted from fires in summers, produces a seasonal variation
139 in all the constituents. It also produces a longitudinal gradient between the Eastern and the Western
140 MB, together with a seasonal variation in the gradient. For example, European anthropogenic
141 emissions were found to significantly influence the Eastern MB surface CO concentrations, while
142 European biomass burning emissions were found to have only a small impact on Eastern MB
143 surface CO concentrations (Drori et al., 2012). Total columns of CH_4 as measured by
144 SCIAMACHY over land and the Eastern Mediterranean from 2003 to 2004 show latitudinal and
145 seasonal variations that cannot be attributed to volcano eruptions (Georgoulias et al., 2011).
146 The aim of the present paper is to assess the variability of CH_4 in the mid-to-upper troposphere
147 between the East and the West of the Mediterranean Basin and to attribute the seasonal variability
148 of the East-West gradient to different processes at both, synoptic and global scales depending on the
149 season and the altitude layer considered. We will study in detail the impact of the summer-time
150 long-range transport of CH_4 from Asia to the Eastern MB through the Asian Monsoon Anticyclone.
151 Since we have already underlined that measurement and modeling of the tropospheric CH_4
152 distribution are challenging, we will adopt a climatological approach and will use a wide variety of
153 space-borne measurements and model outputs to verify that they give consistent results.

We have collected the maximum of information available from satellite measurements and model results in order to study the variability of tropospheric CH_4 over the MB and to assess the processes driving this variability. We have thus built a wide dataset combining all these pieces of information keeping in mind that 1) it is out of the scope of the present paper to perform a validation of satellite products, 2) all these datasets have their own strengths and weaknesses, and 3) the more data we gather, the better the statistics are and furthermore, the dataset consistency can be better assessed. Regarding space-borne measurements, we have considered tropospheric columns of CH_4 from IASI over the period 2008-2011, and upper tropospheric CH_4 profiles from AIRS and GOSAT over the periods 2008-2011 and March-November 2010, respectively. Regarding the models, we have considered three types of chemical models to calculate CH_4 variability in the mid-to-upper troposphere. The MOCAGE (Josse et al., 2004) chemical transport model (CTM), constrained by the ARPEGE meteorological analyses, should a priori give CH_4 vertical profiles more realistic than climate models over a specified period despite the fact that, due to the long lifetime of CH_4, the short spin-up period (3 months vs. 12 years of lifetime) may impact its distribution. On the other hand, chemical climate models (CCMs) as LMDz-OR-INCA (Hauglustaine et al., 2004; Szopa et al., 2013) from the Laboratoire des Sciences du Climat et de l'Environnement (LSCE) and CNRM-AOCCM (Huszar et al., 2013) from Météo-France are run over a much longer period (greater than 10 years) than MOCAGE and should be more adapted to study the climatological variability of CH_4 over the MB. The LMDz-OR-INCA is mainly dedicated to the tropospheric CH_4 profiles since it takes into account the major surface processes that can drive the CH_4 variability in the entire troposphere depending on the inventory scenarios (see section 2.2.3). The CNRM-AOCCM is mainly dedicated to the upper tropospheric-stratospheric CH_4 profiles because it has a detailed description of the stratosphere and should better describe the processes impacting the CH_4 variability in the upper troposphere-lower stratosphere. The 3 models are thus complementary in the study of the CH_4 variability in the mid-to-upper troposphere over the MB.

The manuscript is structured as follow. In section 2, we briefly present the spaceborne instruments and datasets involved in this study, namely MetOp-A/IASI, AQUA/AIRS and GOSAT/TANSO together with the models, namely MOCAGE, CNRM-AOCCM and LMDz-OR-INCA. The meteorology and climatology of CH_4 inferred from the different datasets above the MB are discussed in section 3. The CH_4 variability both in the East and in the West of the MB is presented in section 4. A detailed discussion of the different processes involved in the CH_4 variability above the MB is presented in section 5 underlining the impact of the Asian Monsoon Anticyclone to the distribution of the mid-to-upper CH_4 in the Eastern MB. Finally, section 6 concludes the paper.

2. Datasets

2.1. Satellite data

Our study analyses CH_4 measurements from three different spaceborne TIR sensors (IASI, AIRS and GOSAT) and consider only the pixels over the Mediterranean Sea due to the larger systematic biases over land. The sensitivity of TIR retrievals strongly depends on surface parameters: emissivity, temperature and thermal contrast (Claeyman et al., 2011). The amplitude of diurnal cycle, and its spatial variability, is larger over land than over the sea. Sea surface temperature exhibits a diurnal amplitude weaker than land surface temperature. Therefore, the vertical sensitivity of the TIR measurements, defined as the full-width at half-maximum of the averaging kernels from the optimal estimation method (Rodgers, 2000), over the sea is consistent during day and night and concentrated in the mid-troposphere. Over the land, the vertical sensitivity is, on average, lower in the middle troposphere during the day than during the night, depending on the actual value of the thermal contrast at the surface.

Infrared sounders measurement errors can be rather large, e.g. up to 10% or more for a single CH_4 total column IASI pixel (Turquety et al., 2004). Thus by applying temporal (monthly/seasonally) and geographical averages, including more than a thousand measurements, we

206 can lower the random error to less than 1%. Systematic errors, if any, will of course be unchanged.
207 For that reason, our analysis relies on a differential method to highlight the CH_4 variability by
208 considering the difference between the Eastern MB (EMB) and the Western MB (WMB), assuming
209 that the systematic errors are of the same order of magnitude (although partially unknown) within
210 each geographical box that will be defined in section 3.
211
212 *2.1.1. The IASI data*
213 IASI, on board of MetOp-A, was launched in 2006 by the European Organisation for the
214 Exploitation of Meteorological Satellites (EUMETSAT). More specifications on platform and
215 instrument can be found on http://smsc.cnes.fr/IASI and http://www.eumetsat.int/Home/
216 Main/Satellites/Metop/Instruments/SP_2010053151047495). The retrieval algorithm for CH_4 is
217 based on the neural network theory adapted from Turquety et al. (2004). The retrieval method is
218 embedded in the operational IASI Level 2 product processing facility at EUMETSAT
219 (EUMETSAT, 2004; Schlüssel et al., 2005, August et al., 2012). From the spectral bandwidth
220 1230-1347 cm^{-1}, the estimated accuracy of the CH_4 total column is about 2% and the estimated
221 precision is of the order of 10% (Turquety et al., 2004). The true accuracy cannot be stated without
222 reference to independent means of comparison, which are not available so far. Consequently, we
223 consider a random Gaussian error of ~10% associated with each single pixel of retrieved total
224 column of CH_4. At mid-latitudes, the vertical sensitivity of the total column CH_4 is peaking in the
225 mid-troposphere at ~8 km from 4 to 14 km (Razavi et al., 2009) and, in the tropics, at ~10 km from
226 5 to 15 km. Geophysical level 2 pre-operational data are provided by EUMETSAT (from version 4
227 to version 5 from 2008 to 2011). The CH_4 products, not yet validated, are only experimental
228 products, routinely generated for demonstration and evaluation. Note, the number of daily total
229 columns of CH_4 averaged in a 1°x1° bin is highly variable because of cloud-free IASI
230 considerations. The monthly-averaged IASI data within each of the East and West areas defined in
231 section 3 represent an average of 30000-70000 pixels depending on the month considered.

232

233 *2.1.2. The AIRS data*

234 AIRS is onboard the space platform NASA EOS Aqua, launched in 2002
235 (http://airs.jpl.nasa.gov/). AIRS measures approximately 200 channels in the 7.66 μm absorption
236 band of CH_4, of which 71 channels are used to retrieve CH_4. A detailed description of the retrieval
237 algorithm can be found in Susskind et al. (2011). Note, the averaging kernels provided by NASA
238 will be considered further (section 4.2) in order to degrade the vertical resolution of the model
239 outputs. At mid-latitudes, the most sensitive layer of AIRS channels to CH_4 is at 300 hPa (~9 km)
240 with a vertical sensitivity from 700 to 100 hPa (Xiong et al., 2008), and, in the tropics, at 200 hPa
241 from 500 to 70 hPa consistently with the IASI TIR measurement sensitivity. Around 200-300 hPa,
242 considering the version V5 used in the present analysis (Xiong et al., 2008), the precision of AIRS
243 CH_4 is estimated to be 30 ppbv (1.7%) and validation using in situ aircraft measurements shows
244 that the accuracy of the retrieved CH_4 is 0.5–1.6%. Daily maritime profiles of CH_4 have been
245 averaged in 1°x1° bins over the MB. The monthly-averaged AIRS data within each of the East and
246 West areas defined in section 3 represent an average of 6000-10000 vertical profiles depending on
247 the month considered.

248

249 *2.1.3. The GOSAT data*

250 The Japanese Aerospace Exploration agency (JAXA) launched the GOSAT platform in 2009,
251 with the TANSO-FTS spectrometer, a nadir-viewing instrument designed for greenhouse gases
252 research, CO_2 and CH_4, operating in the TIR and SWIR domains [0.7-14.3 μm] (Kuze et al., 2009).
253 More specifications on platform and instrument can be found on http://www.gosat.nies.go.jp/. The
254 sensitivity of the SWIR CH_4 measurements at 1.67 μm (Yokota et al., 2009) at mid-latitudes over
255 the sea is very weak, thus few meaningful pixels could have been retrieved preventing the use of
256 such information in our analysis. The TIR measurements from Band 4 (5.5–4.3 μm) provide
257 vertical profiles of CH_4 along 7 vertical levels (Imasu et al., 2007) by using the optimal estimation

method with a vertical sensitivity in the tropics peaking at 10 km (higher than at mid-latitudes) from 5 to 15 km (Saitoh et al., 2012), consistently with the vertical sensitivity of IASI (Razavi et al., 2009) and AIRS (Xiong et al., 2008) in the tropics. A selection by using Degree of Freedom of Signal (DFS) is applied for the data having DFS values larger than 0.6 for CH_4. TIR data (L2 Version 0.10) were only available from 16 March to 24 November 2010 from the GOSAT User Interface Gateway at the time the analysis has been performed. These retrievals provide vertical profiles of mixing ratio of CH_4 from 1000 to 100 hPa. Comparisons with aircraft measurements show that the average difference between the GOSAT (TIR) and aircraft CH_4 values (TIR − aircraft) is −5 ppbv, and the 1σ standard deviation is 15 ppbv (Saitoh et al., 2012). Daily maritime profiles of CH_4 have been averaged in 1°x1° bins over the MB. The monthly-averaged GOSAT data within each of the East and West areas defined in section 3 represent an average of 100-300 vertical profiles depending on the month considered, namely 20-30 times less than for AIRS.

2.2. The model data

2.2.1. The MOCAGE data

MOCAGE (MOdèle de Chimie Atmosphérique à Grande Echelle) (Peuch et al., 1999) is a 3D CTM which covers the planetary boundary layer, the free troposphere, and the stratosphere for different applications such as: operational chemical weather forecasting (Dufour et al., 2005); tropospheric and stratospheric research studies (Claeyman et al., 2010; Ricaud et al., 2009); and data assimilation research (El Amraoui et al., 2010; Claeyman et al., 2011). In our study, MOCAGE is forced dynamically by wind and temperature fields from the analyses of the ARPEGE model (Courtier et al., 1991). The MOCAGE horizontal resolution is 2°x2° and the model uses a semi-Lagrangian transport scheme. It includes 47 levels from the surface up to 5 hPa with a vertical resolution of about 800 m around the tropopause, 400-800 m in the troposphere and 40-400 m in the 7 levels of the boundary layer. Chemistry used within MOCAGE is a combination of tropospheric (RACM described in Stockwell et al., 1997) and stratospheric (REPROBUS described in Lefèvre et

al., 1994) chemical schemes. Initial chemical conditions are taken from climatological fields over a spin-up period of 3 months allowing the model to quickly bring chemical fields to realistic spatial distributions. Surface emissions prescribed in MOCAGE are based upon yearly- or monthly-averaged climatologies. More precisely, the CH_4 surface emissions are monthly averages and split into anthropogenic sources taken from the Intergovernmental Panel on Climate Change (IPCC) (Dentener et al., 2005), biomass burning (van de Werf et al., 2003) and biogenic sources (Michou and Peuch, 2002). The CH_4 climatologies are representative of year 2000 for a total emission rate of 534 $Tg(CH_4)$ yr^{-1}.

2.2.2. The CNRM-AOCCM data

The atmospheric model embedded in CNRM-AOCCM is presented in Huszar et al. (2013) based on the Atmosphere-Ocean General Circulation Model (AOGCM) CNRM-CM5 described in Voldoire et al. (2012). The main difference between CNRM-CM5 and CNRM-AOCCM resides in the "online" coupling with a stratospheric chemistry which is based on the REPROBUS scheme. This scheme is applied on the whole vertical column, except between the surface and the 560 hPa level where long-lived chemical species are relaxed towards global average surface value following the A1B scenario from IPCC (2007). The A1B scenario mainly describes a future world of very rapid economic growth, global population that peaks in mid-century and declines thereafter, and the rapid introduction of new and more efficient technologies. Convection of species is not considered. In this chemistry version, the 3-D distribution of the seven absorbing gases (H_2O, CO_2, O_3, CH_4, N_2O, CFC11, and CFC12) is then provided by the chemistry module of CNRM-AOCCM and interacts with the radiative calculations. More details can be found in Michou et al. (2011). In the present version, there are about 50 chemical species, and the horizontal resolution is 2.8°x2.8°. Distribution of atmospheric constituents at the surface are zonally symmetric below 500 hPa (Fig. 10) and greenhouse gases follow the A1B scenario on atmospheric chemistry and climate for the

period of 1940-2100. In the present analysis, for this model, we only consider the climatological period 2001-2010.

2.2.3. The LMDz-OR-INCA data

The INteraction between Chemistry and Aerosol (INCA) model is used to simulate the distribution of aerosols and gaseous reactive species in the troposphere. In the present configuration, the model includes 19 hybrid vertical levels extending up to 4 hPa, and a horizontal resolution of 1.9° in latitude and 3.75° in longitude. INCA is coupled online to the LMDz General Circulation Model (GCM) to account, with different degrees of complexity, for climate chemistry interactions. In the simulations described here, LMDz is coupled with the ORCHIDEE (Organizing Carbon and Hydrology in Dynamic Ecosystems) dynamic global vegetation model (Krinner et al., 2005) for soil/atmosphere exchanges of water and energy (Hourdin et al., 2006), but not for biogenic CO_2 or Volatile Organic Compounds (VOCs) fluxes. Together, these three models form the LMDz-OR-INCA model. Fundamentals for the gas phase chemistry are presented in Hauglustaine et al. (2004) and first results with the full tropospheric gaseous chemical scheme are presented by Folberth et al. (2006). The model includes 223 homogeneous chemical reactions, 43 photolytic reactions and 6 heterogeneous reactions including non-methane hydrocarbon oxidation pathways and aerosol formation. The LMDz-OR-INCA simulation covers four future projections of emissions for the 2000–2100 period. The Representative Concentration Pathways (RCP) emissions are used (Lamarque et al., 2011). They correspond to emission trajectories compatible with the evolution of radiative forcing equivalent in 2100 to 2.6, 4.5, 6.0 and 8.5 Wm^{-2} relative to pre-industrial values (labelled therein after RCP 2.6, 4.5, 6.0 and 8.5). In the present analysis, for this model, we only consider the climatological period 2001-2010.

3. Atmospheric conditions controlling the spatial distribution of methane

Figure 1 shows the CH_4 fields calculated by MOCAGE for summer (June-July-August, JJA) 2009 over the MB at 850, 500 and 200 hPa, superimposed with the wind fields from the ARPEGE analyses averaged over the same period. Figure 2 presents the CH_4 vertical distribution as calculated by MOCAGE in summer 2009 along an East-West axis above the MB. Similarly to Figures 1-2, the Figures 3-4 present, in winter (December-January-February, DJF) 2009, the CH_4 fields as calculated by MOCAGE over the MB at 850, 500 and 200 hPa, and along an East-West axis, respectively. On Figures 2 and 4, the MOCAGE CH_4 fields are superimposed with 1) the wind fields from ARPEGE analyses and 2) the cold point tropopause pressure fields provided by the National Centers for Environmental Prediction (NCEP)/National Center for Atmospheric Research (NCAR) reanalyses, all these data being averaged over the same period.

Considering the meteorology of the MB, we observe two different regimes. 1) In winter (Fig. 3), and more generally from autumn to spring (not shown), from the boundary layer to the upper troposphere, air masses are essentially coming from either Europe or Eastern Atlantic Ocean. 2) In summer (Fig. 1), the meteorology of EMB and WMB is more complex and depends on the altitude considered.

In the planetary boundary layer in summer (Fig. 1, bottom), cells develop in the WMB, and air masses come from Europe, Northern Africa and Eastern Atlantic Ocean, whilst in the EMB, air masses are originated from four major source regions: i) long fetch of maritime European air masses from NW throughout the whole year, ii) North east continental flow originating in south Eastern Europe (Etesian winds) in summer, iii) South-east flow from the Arabian Peninsula occurring in the fall, and iv) South-west flow along the North-African coast most frequent during late winter and spring (Dayan, 1986). In the middle troposphere (Figs. 1 and 3, middle), whatever the season, air masses are essentially coming from the west for both parts of the basin. In summer (Fig. 1, top), upper tropospheric air masses in the WMB are essentially coming from the West, but in the EMB, they are also originated from Northern Africa and the Arabic Peninsula (Ziv et al.,

2004; Liu et al., 2009), and even farther away, from Asia (we will discuss this point in sections 4 and 5). Note that, in summer, the EMB and WMB are also affected by the location of the descending branch of the Hadley cell (Fig. 2). These summer climatologies are all consistent with Millán et al. (1997), Lelieveld et al. (2002), Ziv et al. (2004) and Schicker et al. (2010).

Seasonally-averaged wind fields from ARPEGE analyses show two different regimes in the surface pressure values during the summer (Fig. 1, bottom) and the winter (Fig. 3, bottom) periods. During the summer in the WMB, there is a higher pressure regime than in the EMB (Fig. 1, bottom). In the lowermost troposphere (850 hPa), an anticyclonic cell develops in the WMB that has an impact on the distribution of CH_4 by producing a local minimum (Fig. 1, bottom). At 850 hPa, air masses are coming from Europe, North Africa and the Atlantic Ocean. The CH_4 distribution shows a maximum over Europe, consistently with the strongest emission zones (Fig. 10), and a strong minimum over North Africa. In the mid-troposphere (500 hPa), air masses are coming from Europe, and the Atlantic Ocean (Fig. 1, middle). An East-West gradient is detected with more CH_4 on the EMB. In the upper troposphere (200 hPa) (Fig. 1, top), air masses are originated from the Atlantic Ocean (even North America) and from North Africa and Asia producing over the MB an obvious North-South gradient with more CH_4 in the South (upper troposphere) than in the North (lower stratosphere) attributed to the impact of long-range transport of pollutants (as discussed in section 5). A systematic subsidence is present over the MB (Fig. 2) whatever the longitudinal bin considered due to the presence of semi-permanent subtropical high pressure systems which are centred over the tropical deserts. More precisely, in the WMB, the descent is caused by the presence of a high pressure cell (Fig. 1, bottom) whilst, in the EMB, it is coming from the Hadley cell that is further displaced over the Northern Africa producing a downward branch in the area 30°N-35°N. The tropopause moves up from ~200 hPa in the WMB to ~175 hPa in the EMB (Fig. 2). The CH_4 distribution shows 1) an obvious transition at the tropopause and 2) a minimum in the West and a maximum in the East in the low troposphere

accentuated by the systematic descent in the Eastern MB that brings CH_4-enriched air masses from the upper troposphere to the mid-to-low troposphere.

In winter, the meteorological condition of the MB is much more homogeneous with westerlies blowing whatever the pressure considered from 850 to 200 hPa (Figs. 3-4). North-South (and to a lesser extent East-West) gradients in CH_4 can also be detected (Fig. 3) associated to the local sources of emission over Europe at 850 hPa and to the stratosphere/troposphere transition at 200 hPa. The 500-hPa layer is a transition region between the low and the upper troposphere with minima of CH_4 over North Africa and a cell of high CH_4 in the WMB (Fig. 3, middle). Contrarily to summer, since the temperature of the Mediterranean Sea is greater than that of the surrounding continents, a systematic upward motion is present (Fig. 4) whatever the longitudinal bin considered. The Hadley cell is further displaced to the South (latitude < 30°N) and its downward branch does not affect significantly the EMB. The tropopause pressure is rather stable from the WMB to the EMB, around 260 hPa. The CH_4 distribution shows minimum in the lowermost troposphere and a maximum in the middle troposphere (Fig. 4).

4. CH_4 variability

4.1. CH_4 spatial distribution of the MB

Figure 5 shows the distributions of 1) the CH_4 total columns from IASI over the MB averaged in summer 2009 to compare with the MOCAGE results in time coincidence, and 2) the CH_4 mixing ratios from AIRS at 260 hPa over the MB averaged in summer 2009 to compare with the MOCAGE results at 200 hPa in time coincidence. The measured and modelled data are selected only for the maritime pixels within the boxes [36°N-45°N, 1°E-12°E] and [30°N-37°N, 26°E-37°E] to represent the WMB and the EMB (blue squares in each figure), respectively.

Due to its long lifetime (~12 years), CH_4 is considered as a well-mixed species in the troposphere. Nevertheless the CH_4 spatial distribution over the MB in summer (JJA) 2009 shows some gradients both in the East-West and the North-South directions. Indeed, in the middle

troposphere (inferred from the sensitivity of the IASI total columns) and in the upper troposphere (200-260 hPa), an East-West gradient is observed in the model and satellite data of ~60 ppbv (~4%) in total column and ~30-150 ppbv (~2-9%) in mixing ratio. A North-South gradient is also detected in the MOCAGE and AIRS data but not in the IASI data set. Therefore, there is systematically a maximum of CH_4 from the middle to the upper troposphere in the East of the MB compared to the West. In the mid-to-upper troposphere, these East-West gradients are not originated from the CH_4 sources more intense in Europe than in Northern Africa or in Middle Asia (Fig. 1) but rather from the long-range transport of Asian-origin air masses and the subsidence of air masses in the EMB (Figs. 1-2 and detailed discussion in section 5).

Quantitatively, there is a positive bias in MOCAGE vs. IASI of less than 30 ppbv (2%) in CH_4 total column mixing ratio. The East-West gradient is consistent between IASI and MOCAGE but the North-South modelled gradient is not detected in the IASI data set. In the upper troposphere (200-260 hPa), MOCAGE and AIRS CH_4 mixing ratios are very consistent with gradients more accentuated in the model (~150 ppbv) than in the AIRS data sets (~30 ppbv). A systematic negative bias of MOCAGE compared to AIRS of ~100 ppbv up to 150 ppbv (10%) in the Northern MB is detected. We discuss in the next section the consistency of the vertical profiles of CH_4 measured by the different spaceborne sensors and calculated by MOCAGE together with the associated biases.

4.2. Vertical profiles

Figure 6 shows the vertical profiles of CH_4 as measured by AIRS (750-100 hPa) and GOSAT (1000-100 hPa) and as calculated by MOCAGE (1000-100 hPa) averaged over the EMB and the WMB depending on the four seasons: winter (DJF), spring (March-April-May, MAM), summer (JJA) and autumn (September-October-November, SON) 2010. There is a good agreement to within 20-30 ppbv between AIRS and GOSAT data in the vertical domain 750-200 hPa. GOSAT is systematically greater than AIRS by about 20-30 ppbv for pressure greater than 300 hPa, whilst, for pressure less than 300 hPa, AIRS is systematically greater than GOSAT by 20 ppbv degrading to

50-200 ppbv at 100 hPa. But the shape of the vertical spaceborne profiles is consistent between AIRS and GOSAT. Separately, whatever the season considered, the MOCAGE low-to-mid tropospheric CH_4 is low biased compared to the measured profiles by ~150-200 ppbv. Furthermore, the MOCAGE vertical profiles systematically show a maximum at 300 hPa, that is not present in any of the spaceborne measurements, and a strong decrease above.

In order to assess the impact of the vertical sensitivity of the spaceborne measurements to the CH_4 profiles, we have applied the AIRS averaging kernels, derived from the AIRS retrieval method (Susskind et al., 2011) and provided by NASA for each AIRS pixel, to the profiles calculated by MOCAGE. Note that the AIRS a priori vertical profiles are not used in our study since we are only interested in the vertical shape of the CH_4 profile and not the absolute amount of CH_4. Degrading the vertical resolution of the MOCAGE profiles by the convolution of averaging kernels (Fig. 6) does show a strong impact on the vertical shape of the CH_4 profiles since the strong maximum at 300 hPa is no longer present. Convolved MOCAGE CH_4 profiles are now consistent with AIRS CH_4 profiles whatever the season considered but a systematic low bias of ~150-200 ppbv (8-10%) between AIRS and MOCAGE convolved profiles is observed. This might be due to the fact that no a priori information contributes to the convolved profile. This is also due to the overall underestimation of CH_4 by global models. Indeed, due to coarse horizontal resolution and large uncertainties in the estimated surface emissions, tropospheric CH_4 lifetimes, e.g. evaluated by the multi-model intercomparison project ACCMIP, are about 5-13% lower than observation estimates (Naik et al., 2013; Voulgarakis et al., 2013).

Along the vertical, it is almost impossible to validate the spaceborne profiles with an external data set since, even within the Total Carbon Column Observing Network (http://www.tccon.caltech.edu/) giving accurate and precise column-averaged abundances of CH_4 (Wunch et al., 2010) because no measurement sites are unfortunately available in the vicinity of the MB. Near the surface, the amount of CH_4 is about 1700-1750 ppbv for MOCAGE, and is on average less than the CH_4 GOSAT data by about 150-200 ppbv. At this stage, it is worthwhile

464 considering surface data within the MB. The NOAA Earth System Research Laboratory (ESRL) In
465 Situ Methane Measurements provide some surface CH_4 measurements within and/or in the vicinity
466 of the MB: Lampedusa, Italy (35.52°N, 12.62°E, 45 amsl), Centro de Investigacion de la Baja
467 Atmosfera (CIBA), Spain (41.81°N, 4.93°W, 845 amsl) and Negev Desert, Israel (30.86°N,
468 34.78°E, 477 amsl). On average, these three sites indicate (not shown) a surface CH_4 annual mean
469 of about 1 875 ppbv in 2010, with an annual oscillation of ~20 ppbv amplitude. Consequently, the
470 amount of surface CH_4 in the MOCAGE run for 2010 is actually low biased by about 150-200 ppbv
471 (8-10%) but is very consistent with the LMDz-OR-INCA surface data of ~1725-1750 ppbv over the
472 Mediterranean (Fig. 10). The slight differences between the EMB and the WMB according to the
473 season and height are studied in detail in the next sub-section.
474
475 *4.3. The East-West seasonal variations: measured and calculated differences*
476 The seasonal variations of the differences in CH_4 fields between the EMB and the WMB (i.e.,
477 EMB minus WMB, labelled as "E−W") as measured by AIRS, GOSAT and IASI and as calculated
478 by LMDz-OR-INCA, CNRM-AOCCM and MOCAGE are presented in Figure 7 when considering
479 the upper troposphere (AIRS, GOSAT, LMDz-OR-INCA and CNRM-AOCCM at 260 and 300
480 hPa) and the middle troposphere (IASI and MOCAGE total column mixing ratios). In the middle
481 and upper troposphere (Fig. 7), despite the fact that spaceborne measurements and modelling of
482 CH_4 are challenging, the modelled and measured seasonal variations of E−W are consistent to each
483 other showing a maximum (peak) in summer and a wide minimum in winter.
484 If we consider the time evolution of the total column mixing ratios (namely focussing on the
485 middle troposphere), we note that both MOCAGE and IASI show a maximum in summer, although
486 3 times greater in MOCAGE (~60 ppbv) than in IASI (~20 ppbv) in July and August. The
487 minimum in January-February is close to zero but slightly positive in October (5-10 ppbv). The
488 much stronger maximum in August calculated by MOCAGE compared to IASI CH_4 total columns
489 might be attributable to the sensitivity of spaceborne measurements in the middle troposphere

whilst the MOCAGE tropospheric columns cover the entire troposphere from the surface to the top of the model atmosphere, namely 5 hPa.

In the upper troposphere (300 hPa), the spaceborne instrument datasets show a E–W maximum in summer of ~12 ppbv in August for AIRS and a E–W wide maximum of ~5 ppbv in July-September for GOSAT. A E–W peak of ~10 ppbv in July-August is also calculated by CNRM-AOCCM although, in the LMDz-OR-INCA dataset, the E–W maximum is slightly positive in August (~2 ppbv). The minimum in the satellite datasets is observed in March-April and is negative (from –15 to –20 ppbv) consistently with the LMDz-OR-INCA dataset whilst the CNRM-AOCCM E–W minimum is less intense (–6 ppbv in February and April). The peak-to-peak amplitude of the E–W seasonal variation is almost twice greater in the satellite measurements (~25 ppbv) than in the model data (~15 ppbv). This represents a ~1.5-2.0% variation of CH_4 in the E–W over the entire year. These results suggest that the difference in amplitude between satellite and model in the seasonal evolution of E-W may be due to: a) the comparison technique, the vertical resolution of the models is much better than the vertical resolution of the satellite observations; b) regarding the processes in summer, we may have less CH_4 trapped in the Asian Monsoon Anticyclone redistributed towards the EMB (see section 5) in the models compared to the measurements; c) regarding the processes in winter, since westerlies are mainly present over the MB in the mid-to-upper troposphere (Figs. 3 and 8), we may have too much and/or too rapidly CH_4 transported over the Mediterranean Sea to the East compared to the West, leading to a too smooth E-W gradient in the models compared to the measurements.

We have also to remind that statistically the number of spaceborne measurements used in our analysis (see section 2) is ~5 times greater in IASI compared to AIRS, ~30 times greater in AIRS compared to GOSAT. Consequently, GOSAT monthly-averaged data appear noisier than AIRS monthly-averaged data. Note that IASI total columns are not and cannot be directly compared with AIRS or GOSAT profiles in our analysis. Nevertheless, although IASI data are not operationally produced, the IASI E-W seasonal variation is very consistent with the E-W seasonal variation as

516 deduced from all other datasets. The monthly random error attributed to the E−W IASI CH_4 is about
517 0.1%, much less than the observed peak-to-peak yearly variation. We estimate that the AIRS
518 monthly random error attributed to the E−W CH_4 is twice greater than the one calculated for IASI,
519 and that the GOSAT monthly random error is about 5 times greater than the ones calculated for
520 IASI. We discuss in the next section the origin of the summer peak in the E−W seasonal variation.
521

522 ## 5. Contribution of the Asian Monsoon Anticyclone

523 As stated in sections 3 and 4, interpreting the E−W CH_4 seasonal variation along the vertical
524 requires to consider the distribution of CH_4 over the Asian continent because of the importance of
525 long-range transport. From Rodwell and Hoskins (1996), it is known that there is a meteorological
526 link between monsoons and the dynamics of the deserts and more precisely between the Asian
527 monsoon and the EMB summer regime. The subsidence centre over the EMB owes its location,
528 timing of onset and intensity to the Asian monsoon, and not to the Hadley circulation. Although it
529 takes less than one day to reach the upper troposphere within the Asian monsoon, back-trajectory
530 calculation (Ziv et al., 2004) shows that it takes about 3-4 days for an air parcel to reach and descent
531 the upper tropospheric EMB from the vicinity of the anticyclone that develops over the Asian
532 monsoon. Inside the Asian Monsoon Anticyclone (AMA), pollutants like CO originating from the
533 surface constitute about 50% of the CO concentration at 100 hPa (Park et al., 2009), with the
534 reminder resulting from chemical production in the troposphere. Most of the CO within the AMA
535 comes from India and South East Asia, with an insignificant contribution from the Tibetan Plateau.
536 Randel and Park (2006), and Park et al. (2009) have analyzed in detail this phenomenon over Asia
537 by considering dynamical parameters (potential vorticity) and chemical species (H_2O, CO and O_3).
538 Numerous studies have already evaluated the impact of transport vs. emission of pollutants and
539 aerosols over the MB and its temporal variability considering different pollutants, chemical
540 compounds and aerosols (Wanger et al., 2000; Lelieveld et al., 2002; Pfister et al., 2004; Kallos et

al., 2007). As stated in section 3, two main dynamic factors affect the EMB: 1) the upper to mid-tropospheric subsidence, and 2) the lower-level cool Etesian winds (Ziv et al., 2004). Although the EMB is characterized by strong descent in the middle and upper troposphere in summer, transport from the boundary layer accounts for about 25% of the local Middle Eastern contribution to the ozone enhancement in the middle troposphere (Liu et al., 2009). Elevated CO episodes in EMB during summer can also be attributed to synoptic conditions prone to favorable transport from Turkey and Eastern Europe towards the EMB rather than increased emissions (Drori et al., 2012). Upper tropospheric longitudinal gradients in the EMB of CH_4, CO, hydrocarbons, including acetone, methanol, and acetonitrile, halocarbons, O_3 and total reactive nitrogen (NOy) were also attributed in August 2001 to the chemical impact of the Asian plume (Scheeren et al., 2003). Finally, Georgoulias et al. (2011) present some interesting results of CH_4 from space in the vicinity of the Mediterranean Sea, but only over land and essentially over the Eastern Mediterranean. The authors found, from the total columns of CH_4 as measured by SCIAMACHY in 2003 and 2004, an obvious maximum in August that could not be attributed to any volcano eruptions although this area hosts a significant number of geological formations that could potentially contribute to the total CH_4 burden. Being given that the sensitivity of the SCIAMACHY CH_4 total columns covers the vertical domain 1000-200 hPa from the vertical structure of the averaging kernels presented in Buchwitz et al. (2005), we note that 1) this maximum localized in August is consistent with our study, and 2) the impact of the AMA on the CH_4 fields in the mid-to-upper troposphere cannot be ruled out.

In order to analyze the climalogical impact of the AMA onto the EMB, we have calculated (Fig. 8) the climatological six-day back-trajectories from the point at 33° N, 35° E located in the EMB (red filled circle on Fig. 8) based on the British Atmospheric Data Centre (BADC) trajectory service (http://badc.nerc.ac.uk/community/trajectory/) from 1st July to 31st August (summer convective period) from 2001 to 2010 every 12 hours at 5 different pressure levels: 850 and 700 hPa (lower troposphere), 500 hPa (middle troposphere), and 300 and 200 hPa (upper troposphere). The BADC

567 trajectories were derived from 40-year (ERA40) re-analysis (2.5°x2.5°/pressure levels) produced by
568 the European Centre for Medium-Range Weather Forecasts (ECMWF). The position of the gravity
569 centre of each distribution (i.e. the maximum in the probability distribution function) at each level is
570 represented every 24 hours by a star on Figure 8. This methodology has been firstly used over the
571 Dome C (Concordia) station in Antarctica (Ricaud, 2014). We have also performed the same
572 analysis but for the winter period from 1st January to 31st March 2001-2010 (Fig. 8). Figure 8
573 undoubtedly shows that air parcels above the EMB during the Asian monsoon period of July-
574 August from 2001 to 2010 are originated: a) from Asia in the upper troposphere, b) from Northern
575 America and Northern Africa in the mid-troposphere and c) from Europe in the low troposphere.
576 The same Figure also shows that in winter (and all other seasons but summer, not shown) air parcels
577 above the EMB are originated from the West (Europe, Atlantic Ocean, North America, Pacific
578 Ocean) whatever the pressure level considered from 850 to 100 hPa.

579 We apply the same climatological approach based on the CNRM-AOCCM and LMDz-OR-
580 INCA CH_4 model results over the period 2001-2010. We consider (Fig. 9) the E–W CH_4 seasonal
581 evolution at pressure levels from the lowermost troposphere to the lowermost stratosphere (850,
582 700, 500, 300, 200 and 100 hPa) and different scenarios for LMDz-OR-INCA (RCPs 2.6, 4.5, 6.0
583 and 8.5) in order to check out whether the summer peak still persists. We also represent the fields of
584 CH_4 as specified and/or calculated in the lowermost level (surface level) by CNRM-AOCCM and
585 by LMDz-OR-INCA (4 scenarios) in summer averaged over the climatological period 2001-2010
586 over a wide area covering the MB and the Asian continent in Figure 10, whilst the CH_4 fields
587 calculated at 200 hPa are shown in Figure 11.

588 The E-W CH_4 seasonal variations from the two models (Fig. 9) behave distinctively in the entire
589 troposphere, and agree very well in the lowermost stratosphere. In the lower troposphere (850 and
590 700 hPa), the E–W CH_4 seasonal evolution from LMDz-OR-INCA exhibits a strong semi-annual
591 oscillation of ±10-15 ppbv peaking in winter and summer for the 4 RCPs whilst the evolution from
592 the CNRM-AOCCM shows a weak annual oscillation of 4-5 ppbv amplitude, with a strong

minimum in summer, namely out-of-phase relative to the LMDz-OR-INCA variation. In the middle troposphere at 500 hPa, the 4 LMDz-OR-INCA outputs exhibit a net maximum in August of ~8 ppbv with minima ranging from –2 to –12 ppbv from October to June, whilst the output from CNRM-AOCCM again shows a strong minimum in summer of about –4 ppbv. At this stage, it is important to remind that the two models are Global Circulation Models (GCMs) with an on-line chemistry. The emissions of CH_4 are time-, longitude- and latitude-dependent in LMDz-OR-INCA with surface maxima over the Northern continent (Fig. 10). In CNRM-AOCCM, there is no emission of CH_4 (Fig. 10) but mixing ratios of CH_4 between the surface and the 560 hPa level are relaxed towards evolving global mean surface abundances. This explains why the two models behave separately for pressures greater or equal to 500 hPa. Note that, regarding the shape of the E–W CH_4 seasonal evolution, there is no significant difference within the different scenarios of the LMDz-OR-INCA outputs since surface CH_4 show the same structures independently of the RCPs considered (Fig. 10).

In the upper troposphere (200 and 300 hPa), the outputs from the two models show a peak in summer in the E–W CH_4 seasonal evolution (Fig. 9), but this differs from the RCPs considered for LMDz-OR-INCA. The maximum is much more intense in CNRM-AOCCM (~8 ppbv in July-August and ~30 ppbv in June-July at 300 and 200 hPa, respectively) than in LMDz-OR-INCA (~1 and ~10 ppbv in August for RCP 4.5 but only –4 and +4 ppbv in August for RCP 8.5 at 300 and 200 hPa, respectively; one peak at –4 ppbv in August for RCP 6.0 at 300 hPa but no peak at 200 hPa; no peak for RCP 2.6 neither at 300 nor at 200 hPa). On average, from 500 to 200 hPa, only the RCP 4.5 scenario from LMDz-OR-INCA shows a positive maximum in summer. At 300 and 200 hPa, the LMDz-OR-INCA summer peak is much less intense than the CNRM-AOCCM summer peak.

It is not obvious to understand why the E-W seasonal variation at 200 hPa is positive in summer for RCP 4.5 and not for the other RCPs (except RCP 8.5 in August). The horizontal distribution of CH_4 calculated by the two models at 200 hPa (Fig. 11) drastically differs but local maxima are

centred within the AMA. A zonally-symmetric structure showing a strong South-North gradient in CH_4 is modelled by CNRM-AOCCM with maxima in the tropics (1800 ppbv) and minima at high latitudes (1700 ppbv) and a local maximum centred within the core of the AMA with values greater than 1807 ppbv elongated towards two axis: 1) South-East Asia and 2) Middle East and EMB. The CH_4 field calculated by LMDz-OR-INCA considering the 4 scenarios also shows two maxima over Northern India and over North-East Asia but the horizontal distribution is not zonally-symmetric due to a zonally-asymmetric CH_4 surface field. In all the scenarios considered, the CH_4 maxima within the AMA range from 1710 to 1750 ppbv with increasing RCPs from 2.6 to 8.5. An elongated tongue of enriched CH_4 enters the EMB. More precisely, we can argue that in RCPs 2.6, 6.0 and 8.5, the primary maximum of CH_4 is located northward at 50°N, 135°E (CH_4 values greater than 1720, 1730 and 1750 ppbv, respectively) although it is a secondary maximum in RCP 4.5 (CH_4 values less than 1720 ppbv). Through long-range transport, this mid-latitude maximum is transported Eastward within a band 40°N-50°N enriching CH_4 in the WMB and producing a E-W minimum in summer for RCPs 2.6, 6.0 and 8.5. Since there is a North-South gradient with a maximum in the South for CNRM-AOCCM, CH_4-depleted air masses reach the WMB although CH_4-enriched air masses from the AMA reach the EMB producing a systematic peak in summer, consistently with RCP 4.5.

In the lower stratosphere (100 hPa, Fig. 9), all the model outputs are consistent with each other showing an annual oscillation, with a wide maximum in summer (60-80 ppbv) and a wide minimum in winter (20-35 ppbv). This is apparently surprising keeping in mind that both models significantly differ from the surface (see Fig. 10) to ~500 hPa. But, in the WMB, the 100-hPa pressure corresponds to 420-K potential temperature both in summer (Fig. 2) and in winter (Fig. 4) whilst, in the EMB, it corresponds to 390 K in summer and 400 K in winter, namely closer to the tropopause in summer than in winter. Consequently, whatever the model considered, the E-W CH_4 seasonal variation at 100 hPa a) is always positive and b) shows a peak in the summer period. We note that the summer peak in E–W seasonal evolution from the middle to the upper troposphere has also been

observed and calculated by considering other constituents like CO and O_3 (not shown). This is the main topic of a forthcoming paper.

In conclusion, a schematic representation of the summertime processes impacting mid-to-upper CH_4 in the EMB is presented in Figure 12. In our study, whatever the amount of CH_4 at the surface and its horizontal distribution, 1850-2000 ppbv for LMDz-OR-INCA consistently with the emission sources (Asia, Northern and Eastern Europe, Central Africa) or 1820 ppbv uniformly spread (Fig. 10), the Asian monsoon traps elevated amounts of CH_4 that converge through the depression, and are uplifted up to the upper troposphere at 200 hPa (Fig. 11) where they build up. At this level, the AMA re-distributes elevated amounts of CH_4 towards Middle East, North Africa and the EMB through long-range transport. Finally, elevated amounts of CH_4 build up in the EMB where they descend to the middle troposphere.

6. Conclusions

The present study is part of the Chemical and Aerosol Mediterranean Experiment (ChArMEx) programme. The aim is to investigate the tropospheric CH_4 time and space variations above the Mediterranean Basin (MB) and to attribute the variability to differing synoptic and global scales depending on the season and the altitude layer considered. Since the analysis of the mid-to-upper tropospheric CH_4 distribution from spaceborne sensors and model outputs is challenging, we have used a wide variety of datasets. 1) The spaceborne measurements from Thermal Infrared (TIR) instruments: Thermal And Near infrared Sensor for carbon Observations - Fourier Transform Spectrometer (TANSO-FTS) instrument on the Greenhouse gases Observing SATellite (GOSAT) satellite, the Atmospheric InfraRed Spectrometer (AIRS) on the Aura platform and the Infrared Atmospheric Sounder Interferometer (IASI) instrument aboard the MetOp-A platform. 2) The model results from the Chemical Transport Model (CTM) MOCAGE, and the two Chemical Climate Models (CCMs) CNRM-AOCCM and LMDz-OR-INCA (the later considering different emission scenarios, RCPs 2.6, 4.5, 6.0 and 8.5).

671 Since CH_4 is a long-lived tracer with lifetime of ~12 years and is supposed to be well mixed in
672 the troposphere, we had to adopt a climatological approach to highlight the weak expected
673 variability. Spaceborne measurements and the model results were selected and monthly-averaged
674 only over the Mediterranean Sea. The period under interest spans from 2008 to 2011 for the satellite
675 measurements and the MOCAGE model results whilst, regarding the CCMs, we have averaged the
676 model outputs over the climatological period from 2001 to 2010.

677 From both satellite and model results, our study obviously demonstrates the persistence of an
678 East-West gradient in CH_4 from the middle to the upper troposphere with a maximum in the
679 Western MB whatever the season considered except in summer when larger amounts of CH_4
680 accumulate above the Eastern MB. In winter, air masses mainly originating from Atlantic Ocean
681 and Europe tend to favour an elevated amount of mid-to-upper tropospheric CH_4 in the West
682 compared to the East of the MB, with a general upward transport above the MB. In summer, the
683 meteorological condition of the MB is changed, favouring air from Northern Africa and Middle
684 East together with Atlantic Ocean and Europe, with a general descent above the Eastern MB.

685 Our analysis shows that, in the upper troposphere (300 hPa), the peak-to-peak amplitude of the
686 East–West seasonal variation in CH_4 above the MB is weak but almost twice greater in the satellite
687 measurements (~25 ppbv) than in the model data (~15 ppbv).. The maximum of CH_4 in summer
688 above the Eastern MB can be explained by a series of dynamical processes only occurring in
689 summer. The Asian monsoon traps and uplifts high amounts of CH_4 to the upper troposphere where
690 they build up. The Asia monsoon Anticyclone redistributes these elevated CH_4 amounts towards
691 North Africa and Middle East to finally reach and descent in the Eastern MB. Consequently, the
692 seasonal variation of the difference in CH_4 between the East and the West MB shows a maximum in
693 summer for pressures from 500 to 100 hPa considering both spaceborne measurements and model
694 results whatever the emission scenarios used for the CCMs. But only the RCP 4.5 scenario gives
695 systematically a positive summer peak whatever the pressure level considered, consistently with the
696 measurements.

From this study, we conclude that CH_4 in the mid-to-upper troposphere over the MB is mainly affected by long-range transport, particularly intense in summer from Asia. Conversely, in the lower troposphere, the CH_4 variability is driven by the local sources of emission in the vicinity of the MB. Other constituents can also be affected by this summer mechanism e.g. O_3 and CO (not shown). In a forthcoming paper, the time evolution of the CH_4, O_3 and CO fields above the MB and at the Asian scale is being studied by considering the outputs from different CCMs in the contemporary period (2000-2010) in order to study the future evolution of the chemical climate over the MB by 2100. Finally, despite the fact that IASI CH_4 data as delivered by EUMETSAT are not operational, the seasonal variation of the East-West difference in CH_4 total columns is nevertheless consistent with theoretical results and measurements from AIRS and IASI.

Acknowledgments. We would like to thank the following institutes and programme for funding our study: Centre National de la Recherche Scientifique-Institut National des Sciences de l'Univers/CNRS-INSU, Centre National des Etudes Spatiales/CNES, Agence de l'Environnement et de la Maîtrise del'Energie/ADEME through the programme the Mediterranean Integrated STudies at Regional And Local Scales/MISTRALS Chemistry-Aerosol Mediterranean Experiment/ChArMEx. We also thank the following data bases for accessing the data: the French database Ether, the European Organisation for the Exploitation of Meteorological Satellites, the GOSAT User Interface Gateway, the National Oceanic and Atmospheric Administration, the British Atmospheric Data Centre to access the LMDz-OR-INCA model data through the international Atmospheric Chemistry and Climate Model Intercomparison Project initiative, and the Global Atmosphere Watch from the World Meteorological Organization. Thanks to the British Atmospheric Data Centre, which is part of the Natural Environment Research Council (NERC) National Centre for Atmospheric Science (NCAS), for the calculation of trajectories and access to European Centre for Medium-Range Weather Forecasts (ECMWF) data. We finally would like to thank the two anonymous reviewers for their fruitful comments.

References

August, T., Klaes, D., Schlüssel, P., Hultberg, T., Crapeau, M., Arriaga, A., O'Carroll, A., Coppens, D., Munro, R., and Calbet, X.: IASI on Metop-A: Operational Level 2 retrievals after five years in orbit, J. Quant. Spectrosc. Rad. Transfer, 113:11, 1340-1371, 2012.

Bergamaschi, P., Frankenberg, C., Fokke Meirink, J., Krol, M., Villani, M. G., Houweling, S., Dentener, F., Dlugokencky, E. J., Miller, J. B., Gatti, L. V., Engel, A., and Levin, I.: Inverse modeling of global and regional CH4 emissions using SCIAMACHY satellite retrievals, J. Geophys. Res., 114, D22301, doi:10.1029/2009JD012287, 2009.

Bousquet, P., Ringeval, B., Pison, I., Dlugokencky, E. J., Brunke, E.-G., Carouge, C., Chevallier, F., Fortems-Cheiney, A., Frankenberg, C., Hauglustaine, D. A., Krummel, P. B., Langenfelds, R. L., Ramonet, M., Schmidt, M., Steele, L. P., Szopa, S., Yver, C., Viovy, N., and Ciais, P.: Source attribution of the changes in atmospheric methane for 2006–2008, Atmos. Chem. Phys., 11, 3689-3700, doi:10.5194/acp-11-3689-2011, 2011.

Buchwitz, M., Rozanov, V. V., and Burrows, J. P.: A near-infrared optimized DOAS method for the fast global retrieval of atmospheric CH4, CO, CO2, H2O, and N2O total column amounts from SCIAMACHY Envisat-1 nadir radiances, J. Geophys. Res., 105(D12), 15231–15245, doi:10.1029/2000JD900191, 2000.

Buchwitz, M., de Beek, R., Burrows, J. P., Bovensmann, H., Warneke, T., Notholt, J., Meirink, J. F., Goede, A. P. H., Bergamaschi, P., Körner, S., Heimann, M., and Schulz, A.: Atmospheric methane and carbon dioxide from SCIAMACHY satellite data: initial comparison with chemistry and transport models, Atmos. Chem. Phys., 5, 941-962, doi:10.5194/acp-5-941-2005, 2005.

Cristofanelli, P., Fierli, F., Marinoni, A., Calzolari, F., Duchi, R., Burkhart, J., Stohl, A., Maione, M., Arduini, J., and Bonasoni, P.: Influence of biomass burning and anthropogenic emissions on ozone, carbon monoxide and black carbon at the Mt. Cimone GAW-WMO global station (Italy, 2165 m asl), Atmos. Chem. Phys., 13, 15-30, doi:10.5194/acp-13-15-2013, 2013.

749 Christoudias, T., Pozzer, A., and Lelieveld, J.: Influence of the North Atlantic Oscillation on air
750 pollution transport. Atmos. Chem. Phys., 12, 869-877, doi:10.5194/acp-12-869-2012, 2012.
751 Claeyman, M., Attié, J.-L., El Amraoui, L., Cariolle, D., Peuch, V.-H., Teyssèdre, H., Josse, B.,
752 Ricaud, P., Massart, S., Piacentini, A., Cammas, J.-P., Livesey, N. J., Pumphrey, H. C., and
753 Edwards, D. P.: A linear CO chemistry parameterization in chemistry-transport models:
754 evaluation and application to data assimilation, Atmos. Chem. Phys., 10, 6097-6115, 2010.
755 Claeyman, M., Attié, J.-L., Peuch, V.-H., El Amraoui, L., Lahoz, W. A., Josse, B., Ricaud, P., von
756 Clarmann, T., Höpfner, M., Orphal, J., Flaud, J.-M., Edwards, D. P., Chance, K., Liu, X.,
757 Pasternak, F., and Cantié, R.: A geostationary thermal infrared sensor to monitor the lowermost
758 troposphere: O_3 and CO retrieval studies, Atmos. Meas. Tech., 4, 297-317, 2011.
759 Clerbaux, C., Chazette, P., Hadji-Lazaro, J., Mégie, G., Müller, J.-F., and Clough, S. A.: Remote
760 sensing of CO, CH4, and O3 using a spaceborne nadir-viewing interferometer, J. Geophys. Res.,
761 103, 18999–19013, doi:10.1029/98JD01422, 1998.
762 Courtier, P., Freydier, C., Geleyn, J. F., Rabier, F., and Rochas, M.: The ARPEGE project at
763 METEO-FRANCE. In: Proc ECMWF Workshop. Numerical methods in atmospheric modelling,
764 9–13 Sept 1991, 2, 193–231. ECMWF, Shinfield Park, Reading, UK, 1991.
765 Crevoisier, C., Nobileau, D., Armante, R., Crépeau, L., Machida, T., Sawa, Y., Matsueda, H.,
766 Schuck, T., Thonat, T., Pernin, J., Scott, N. A., and Chédin, A.: The 2007–2011 evolution of
767 tropical methane in the mid-troposphere as seen from space by MetOp-A/IASI, Atmos. Chem.
768 Phys., 13, 4279-4289, doi:10.5194/acp-13-4279-2013, 2013.
769 Cros, B., Durand, P., and Cachier, H.: An overview of the ESCOMPTE campaign, Atmos. Res,
770 69(3-4), 241-279, 2004.
771 Dayan, U.: Climatology of Back Trajectories from Israel Based on Synoptic Analysis. J. Climate
772 Appl. Meteor., 25, 591–595. doi: http://dx.doi.org/10.1175/1520-0450(1986), 1986.
773 Dentener, F., Stevenson, D., Cofala, J., Mechler, R., Amann, M., Bergamaschi, P., Raes, F., and
774 Derwent, R.: The impact of air pollutant and methane emission controls on tropospheric ozone

775 and radiative forcing: CTM calculations for the period 1990–2030, Atmos. Chem. Phys., 5,
776 1731–1755, http://www.atmos-chem-phys.net/5/1731/2005/, 2005.
777 Drori, R., Dayan, U., Edwards, D. P., Emmons, L. K., and Erlick, C.: Attributing and quantifying
778 carbon monoxide sources affecting the Eastern Mediterranean: a combined satellite, modelling,
779 and synoptic analysis study, Atmos. Chem. Phys., 12, 1067-1082, doi:10.5194/acp-12-1067-
780 2012, 2012.
781 Dufour, A., Amodei, M., Ancellet, G., and Peuch, V.-H.: Observed and modelled "chemical
782 weather" during ESCOMPTE, Atmos. Res., 74, 161–189, 2005.
783 El Amraoui, L., Attié, J.-L., Semane, N., Claeyman, M., Peuch, V.-H., Warner, J., Ricaud, P.,
784 Cammas, J.-P., Piacentini, A., Cariolle, D., Massart, S., and Bencherif, H.: Midlatitude
785 stratosphere – troposphere exchange as diagnosed by MLS O3 and MOPITT CO assimilated
786 fields, Atmos. Chem. Phys., 10, 2175-2194, 2010.
787 EUMETSAT, IASI Level 2 Products Guide, EUM/OPS-EPS/MAN/04/0033. Available on
788 http://oiswww.eumetsat.org/WEBOPS/eps-pg/IASI-L2/IASIL2-PG-0TOC.htm, 2004.
789 Folberth, G. A., Hauglustaine, D. A., Lathière, J., and Brocheton, F.: Interactive chemistry in the
790 Laboratoire de Météorologie Dynamique general circulation model: model description and
791 impact analysis of biogenic hydrocarbons on tropospheric chemistry, Atmos. Chem. Phys.,
792 6:2273–2319. www.atmos-chem-phys.net/6/2273/2006/, 2006.
793 Georgoulias, A. K., Kourtidis, K. A., Buchwitz, M., Schneising, O., and Burrows, J. P.: A case
794 study on the application of SCIAMACHY satellite methane measurements for regional studies:
795 the Greater Area of Eastern Mediterranean, Int. J. Remote Sens., 32(3), 787-813,
796 doi:10.1080/01431161.2010.517791, 2011.
797 Giorgi, F., and Lionello, P.: Climate change projections for the Mediterranean region, Global and
798 Planetary Change, 63(2), 90–104, doi:10.1016/j.gloplacha.2007.09.005, 2008.
799 Hauglustaine, D. A., Hourdin, F., Jourdain, L., Filiberti, M.-A., Walters, S., Lamarque, J.-F., and
800 Holland, E. A.: Interactive chemistry in the Laboratoire de Meteorologie Dynamique general

801 circulation model: description and background tropospheric chemistry evaluation, J. Geophys.
802 Res., 109:D04314. doi:10.1029/2003JD003957, 2004.
803 Hilton, F., Armante, R., August, T., Barnet, C., Bouchard, A., Camy-Peyret, C., Capelle, V.,
804 Clarisse, L., Clerbaux, C., Coheur, P.-F., Collard, A., Crevoisier, C., Dufour, G., Edwards, D.,
805 Faijan, F., Fourrié, N., Gambacorta, A., Goldberg, M., Guidard, V., Hurtmans, D., Illingworth,
806 S., Jacquinet-Husson, N., Kerzenmacher, T., Klaes, D., Lavanant, L., Masiello, G., Matricardi,
807 M., McNally, A., Newman, S., Pavelin, E., Payan, S., Péquignot, E., Peyridieu, S., Phulpin, T.,
808 Remedios, J., Schlüssel, P., Serio, C., Strow, L., Stubenrauch, C., Taylor, J., Tobin, D., Wolf,
809 W., and Zhou, D.: Hyperspectral Earth Observation from IASI: Five Years of Accomplishments,
810 B. Am. Meteor. Soc., 93, 347–370, doi:10.1175/BAMS-D-11-00027.1, 2012.
811 Hourdin, F., Musat, I., Bony, S., Braconnot, P., Codron, F., Dufresne, J.-L., Fairhead, L., Filiberti,
812 M.-A., Friedlingstein, P., Grandpeix, J.-Y., Krinner, G., LeVan, P., Li, Z.-X., and Lott, F.: The
813 LMDZ4 general circulation model: climate performance and sensitivity to parametrized physics
814 with emphasis on tropical convection, Clim. Dyn., 27, 787–813, doi:10.1007/s00382-006-0158-
815 0, 2006.
816 Huszar, P., Teyssèdre, H., Cariolle, D., Olivié, D. J. L., Michou, M., Saint-Martin, D., Senesi, S.,
817 Voldoire, A., Salas y Melia, D., Alias, A., Karcher, F., Ricaud, P., and Halenka, T.: Modeling
818 the present and future impact of aviation on climate: an AOGCM approach with online coupled
819 chemistry, Atmos. Chem. Phys., 13, 10027-10048, doi:10.5194/acp-13-10027-2013, 2013.
820 Im, U. and Kanakidou, M.: Impacts of East Mediterranean megacity emissions on air quality,
821 Atmos. Chem. Phys., 12, 6335-6355, doi:10.5194/acp-12-6335-2012, 2012.
822 Imasu, R., Saitoh, N., and Niwa, Y.: Retrieval performance of GOSAT thermal infrared FTS sensor
823 for measuring CO_2 concentrations, Proc. SPIE 6744, Sensors, Systems, and Next-Generation
824 Satellites XI, 67440F, http://dx.doi.org/10.1117/12.737796, 2007.

825 IPCC: Climate change 2007: The physical science basis. Contribution of working group I to the
826 fourth assessment report of the intergovernmental panel on climate change, Cambridge, UK and
827 New York, USA, Cambridge University Press, 996 pp., 2007.
828 Josse, B., Simon, P., and Peuch, V.-H.: Rn−222 global simulations with the multiscale CTM
829 MOCAGE, Tellus, 56B, 339–356, 2004.
830 Kallos, G., Astitha, M., Katsafados, P., and Spyrou, C.: Long-Range Transport of
831 Anthropogenically and Naturally Produced Particulate Matter in the Mediterranean and North
832 Atlantic: Current State of Knowledge, J. Appl. Meteorol. Clim., 46, 1230-1251, 2007.
833 Kanakidou, M., Mihalopoulos, N., Kindap, T., Im, U., Vrekoussis, M., Gerasopoulos, E.,
834 Dermitzaki, E., Unal, A., Kocak, M., Markakis, K., Melas, D., Kouvarakis, G., Youssef, A. F.,
835 Richter, A., Hatzianastassiou, N., Hilboll, A., Ebojie, F., von Savigny, C., Ladstaetter-
836 Weissenmayer, A., Burrows, J., and Moubasher, H.: Megacities as hot spots of air pollution in
837 the East Mediterranean, Atmos. Environ., 45, 1223–1235, 2011.
838 Krinner, G., Viovy, N., de Noblet-Ducoudré, N., Ogée, J., Polcher, J., Friedlingstein, P., Ciais, P.,
839 Sitch, S., and Prentice, I. C.: A dynamic global vegetation model for studies of the coupled
840 atmosphere-biosphere system, Global Biogeochem. Cycles, 19, GB1015,
841 doi:10.1029/2003GB002199, 2005.
842 Kuze, A., Suto, H., Nakajima, M., and Hamazaki, T.: Thermal and near infrared sensor for carbon
843 observation Fourier-transform spectrometer on the Greenhouse Gases Observing Satellite for
844 greenhouse gases monitoring, Appl. Opt., 48, 6716-6733, 2009.
845 Ladstätter-Weißenmayer, A., Heland, J., Kormann, R., von Kuhlmann, R., Lawrence, M. G.,
846 Meyer-Arnek, J., Richter, A., Wittrock, F., Ziereis, H., and Burrows, J.-P.: Transport and build-
847 up of tropospheric trace gases during the MINOS campaign: comparison of GOME, in situ
848 aircraft measurements and MATCH-MPIC-data, Atmos. Chem. Phys., 3, 1887–1902, 2003.
849 Lamarque, J.-F., Kyle, G. P., Meinshausen, M., Riahi, K., Smith, S. J., van Vuuren, D. P., Conley,
850 A. J., and Vitt, F.: Global and regional evolution of short-lived radiatively-active gases and

aerosols in the Representative Concentration Pathways, Climatic Change, 109:191–212 DOI 10.1007/s10584-011-0155-0, 2011.

Lamarque, J.-F., Shindell, D. T., Josse, B., Young, P. J., Cionni, I., Eyring, V., Bergmann, D., Cameron-Smith, P., Collins, W. J., Doherty, R., Dalsoren, S., Faluvegi, G., Folberth, G., Ghan, S. J., Horowitz, L. W., Lee, Y. H., MacKenzie, I. A., Nagashima, T., Naik, V., Plummer, D., Righi, M., Rumbold, S. T., Schulz, M., Skeie, R. B., Stevenson, D. S., Strode, S., Sudo, K., Szopa, S., Voulgarakis, A., and Zeng, G.: The Atmospheric Chemistry and Climate Model Intercomparison Project (ACCMIP): overview and description of models, simulations and climate diagnostics, Geosci. Model Dev., 6, 179-206, 2013.

Lefèvre, F., Brasseur, G. P., Folkins, I., Smith, A. K., and Simon, P.: Chemistry of the 1991–1992 stratospheric winter: Three-dimensional model simulations, J. Geophys. Res., 99, 9183–8195, 1994.

Lelieveld, J., Berresheim, H., Borrmann, S., Crutzen, P. J., Dentener, F. J., Fischer, H., Feichter, J., Flatau, P. J., Heland, J., Holzinger, R., Korrmann, R., Lawrence, M. G., Levin, Z., Markowicz, K. M., Mihalopoulos, N., Minikin, A., Ramanathan, V., de Reus, M., Roelofs, G. J., Scheeren, H. A., Sciare, J., Schlager, H., Schultz, M., Siegmund, P., Steil, B., Stephanou, E. G., Stier, P., Traub, M., Warneke, C., Williams, J., and Ziereis, H.: Global Air Pollution Crossroads over the Mediterranean, Science, 298, 5594, 794-799, DOI: 10.1126/science.1075457, 2002.

Lionello, P. (Ed.): The Climate of the Mediterranean Region: From the past to the future. 592p, Elsevier, 2012.

Liu, J. J., Jones, D. B. A., Worden, J. R., Noone, D., Parrington, M., and Kar, J.: Analysis of the summertime buildup of tropospheric ozone abundances over the Middle East and North Africa as observed by the Tropospheric Emission Spectrometer instrument, J. Geophys. Res., 114, D05304, doi:10.1029/2008JD010993, 2009.

875 Masson, O., Piga, D., Gurriaran, R., and D'Amico, D.: Impact of an exceptional Saharan dust
876 outbreak in France: PM10 and artificial radionuclides concentrations in air and in dust deposit,
877 Atmos. Env., 44, 20, 2478–2486, http://dx.doi.org/10.1016/j.atmosenv.2010.03.004, 2010.
878 Michou, M., and Peuch, V.-H.: Surface exchanges in the MOCAGE multiscale Chemistry and
879 Transport Model, J. Water Sci., 15, 173–203, 2002.
880 Michou, M., Saint-Martin, D., Teyssèdre, H., Alias, A., Karcher, F., Olivié, D., Voldoire, A., Josse,
881 B., Peuch, V.-H., Clark, H., Lee, J. N., and Cheroux, F.: A new version of the CNRM
882 Chemistry-Climate Model, CNRM-CCM: description and improvements from the CCMVal-2
883 simulations, Geosci. Model Dev., 4, 873–900, doi:10.5194/gmd-4-873-2011, 2011.
884 Millán, M. M., Salvador, R., Mantilla, E., and Kallos, G.: Photooxidant dynamics in the
885 Mediterranean basin in summer: Results from European research projects, J. Geophys. Res., 102,
886 8811–8823, doi:10.1029/96JD03610, 1997.
887 Nabat, P., Solmon, F., Mallet, M., Kok, J. F., and Somot, S.: Dust emission size distribution impact
888 on aerosol budget and radiative forcing over the Mediterranean region: a regional climate model
889 approach, Atmos. Chem. Phys., 12, 10545-10567, 2012.
890 Naik, V., Voulgarakis, A., Fiore, A. M., Horowitz, L. W., Lamarque, J.-F., Lin, M., Prather, M. J.,
891 Young, P. J., Bergmann, D., Cameron-Smith, P. J., Cionni, I., Collins, W. J., Dalsøren, S. B.,
892 Doherty, R., Eyring, V., Faluvegi, G., Folberth, G. A., Josse, B., Lee, Y. H., MacKenzie, I. A.,
893 Nagashima, T., van Noije, T. P. C., Plummer, D. A., Righi, M., Rumbold, S. T., Skeie, R.,
894 Shindell, D. T., Stevenson, D. S., Strode, S., Sudo, K., Szopa, S., and Zeng, G.: Preindustrial to
895 present-day changes in tropospheric hydroxyl radical and methane lifetime from the
896 Atmospheric Chemistry and Climate Model Intercomparison Project (ACCMIP), Atmos. Chem.
897 Phys., 13, 5277-5298, doi:10.5194/acp-13-5277-2013, 2013.
898 Park, M., Randel, W. J., Emmons, L. K., and Livesey, N. J.: Transport pathways of carbon
899 monoxide in the Asian summer monsoon diagnosed from Model of Ozone and Related Tracers
900 (MOZART), J. Geophys. Res., 114, D08303, doi:10.1029/2008JD010621, 2009.

Peuch, V.-H., Amodei, M., Barthet, T., Cathala, M.-L., Josse, B., Michou, M., and Simon, P. : MOCAGE: Modèle de Chimie, Atmosphérique A Grande Echelle, Actes des Atelier de Modélisation de l'Atmosphère, Météo-France, 33–36, 1999.

Pfister, G., Petron, G., Emmons, L. K., Gille, J. C., Edwards, D. P., Lamarque, J.-F., J.-L. Attié, C. Granier, and Novelli, P. C: Evaluation of CO simulations and the analysis of the CO budget for Europe, J. Geophys. Res.-Atmos. (1984–2012), 109(D19), 2004.

Randel, W. J., and Park, M.: Deep convective influence on the Asian summer monsoon anticyclone and associated tracer variability observed with Atmospheric Infrared Sounder (AIRS), J. Geophys. Res., 111, D12314, doi:10.1029/2005JD006490, 2006.

Razavi, A., Clerbaux, C., Wespes, C., Clarisse, L., Hurtmans, D., Payan, S., Camy-Peyret, C., and Coheur, P. F.: Characterization of methane retrievals from the IASI space-borne sounder, Atmos. Chem. Phys., 9, 7889–7899, 2009.

Ricaud, P., Attié, J.-L., Teyssèdre, H., El Amraoui, L., Peuch, V.-H., Matricardi, M., and Schluessel, P.: Equatorial total column of nitrous oxide as measured by IASI on MetOp-A: implications for transport processes, Atmos. Chem. Phys., 9, 3947-3956, doi:10.5194/acp-9-3947-2009, 2009.

Ricaud, P.: Variabilités de la vapeur d'eau et de la température troposphérique mesurées par le radiomètre micro-onde HAMSTRAD au Dôme C, Antarctique. Partie II : Résultats scientifiques, La Météorologie, 85, 35-46, doi: 10.4267/2042/53749, 2014.

Rodgers, C. D., *Inverse Methods for Atmospheric Sounding: Theory and Practice*, 1st ed. Singapore: World Scientific, 2000.

Rodwell, M. J., and Hoskins, B. J.: Monsoons and the dynamics of deserts, Q. J. R. Meteorol. Soc., 122, 1385-1404, 1996.

Saitoh, N., Touno, M., Hayashida, S., Imasu, R., Shiomi, K., Yokota, T., Yoshida, Y., Machida, T., Matsueda, H., and Sawa, Y.: Comparisons between XCH_4 from GOSAT Shortwave and Thermal

926 Infrared Spectra and Aircraft CH_4 Measurements over Guam, SOLA, 8, 145−149,
927 doi:10.2151/sola.2012-036, 2012.
928 Scheeren, H. A., Lelieveld, J., Roelofs, G. J., Williams, J., Fischer, H., de Reus, M., de Gouw, J. A.,
929 Bolder, M., van der Veen, C., and Lawrence, M.: The impact of monsoon outflow from India
930 and Southeast Asia in the upper troposphere over the eastern Mediterranean, Atmos. Chem.
931 Phys., 3, 1589–1608, 2003.
932 Schicker, I., Radanovics, S., and Seibert, P.: Origin and transport of Mediterranean moisture and
933 air, Atmos. Chem. Phys., 10, 5089-5105, doi:10.5194/acp-10-5089-2010, 2010.
934 Scheeren, H. A., Lelieveld, J., Roelofs, G. J., Williams, J., Fischer, H., de Reus, M., de Gouw, J. A.,
935 Warneke, C., Holzinger, R., Schlager, H., Klüpfel, T., Bolder, M., van der Veen, C., and
936 Lawrence, M.: The impact of monsoon outflow from India and Southeast Asia in the upper
937 troposphere over the eastern Mediterranean, Atmos. Chem. Phys., 3, 1589-1608,
938 doi:10.5194/acp-3-1589-2003, 2003.
939 Schlüssel, P., Hultberg, T. H., Phillips, P. L., August, T., and Calbet, X.: The operational IASI
940 Level 2 Processor, Adv. Space Res., 36, 982-988, 2005.
941 Stockwell, W. R., Kirchner, F., Kuhn, M., and Seefeld, S.: A new mechanism for regional
942 atmospheric chemistry modelling, J. Geophys. Res.: Atmospheres (1984–2012), 102(D22),
943 25847-25879, 1997.
944 Susskind, J., Blaisdell, J. M., Iredell, L. and Keita, F.: Improved Temperature Sounding and Quality
945 Control Methodology Using AIRS/AMSU Data: The AIRS Science Team Version 5 Retrieval
946 Algorithm, IEEE Trans. Geosc. Remote Sens., 49, 883-907, 2011.
947 Szopa, S., Balkanski, Y., Schulz, M., Bekki, S., Cugnet, D., Fortems-Cheiney, A., Turquety, S.,
948 Cozic, A., Déandreis, C., Hauglustaine, D., Idelkadi, A., Lathière, J., Lefèvre, F., Marchand, M.,
949 Vuolo, R., Yan, N., and Dufresne, J.-L.: Aerosol and ozone changes as forcing for climate
950 evolution between 1850 and 2100, Clim. Dynam., 40, 2223-2250, 2013. DOI:10.1007/s00382-
951 012-1408-y

952 Turquety, S., Hadji-Lazaro, J., Clerbaux, C., Hauglustaine, D. A., Clough, S. A., Cassé, V.,
953 Schlüssel, P., and Mégie, G.: Operational trace gas retrieval algorithm for the Infrared
954 Atmospheric Sounding Interferometer, J. Geophys. Res., 109, D21301,
955 doi:10.1029/2004JD004821, 2004.
956 van der Werf, G. R., Randerson, J. T., Collatz, G. J., and Giglio, L.: Carbon emissions from fires in
957 tropical and subtropical ecosystems, Global Change Biol., 9, 547–562, 2003.
958 Voldoire, A., Sanchez-Gomez, E., Salas y Melia, D., Decharme, B., Cassou, C., Sénési, S., Valcke,
959 S., Beau, I., Alias, A., Chevallier, M., Deque, M., Deshayes, J., Douville, H., Fernandez, E.,
960 Madec, G., Maisonnave, E., Moine, M.-P., Planton, S., Saint-Martin, D., Szopa, S., Tyteca, S.,
961 Alkama, R., Belamari, S., Braun, A., Coquart, L., and Chauvin, F.: The CNRM-CM5.1 global
962 climate model: description and basic evaluation, Clim. Dynam., doi:10.1007/s00382-011-1259-
963 y, 2012.
964 Voulgarakis, A., Naik, V., Lamarque, J.-F., Shindell, D. T., Young, P. J., Prather, M. J., Wild, O.,
965 Field, R. D., Bergmann, D., Cameron-Smith, P., Cionni, I., Collins, W. J., Dalsøren, S. B.,
966 Doherty, R. M., Eyring, V., Faluvegi, G., Folberth, G. A., Horowitz, L. W., Josse, B.,
967 MacKenzie, I. A., Nagashima, T., Plummer, D. A., Righi, M., Rumbold, S. T., Stevenson, D. S.,
968 Strode, S. A., Sudo, K., Szopa, S., and Zeng, G.: Analysis of present day and future OH and
969 methane lifetime in the ACCMIP simulations, Atmos. Chem. Phys., 13, 2563-2587,
970 doi:10.5194/acp-13-2563-2013, 2013.
971 Wanger, A., Peleg, M., Sharf, G., Mahrer, Y., Dayan, U., Kallos, G., Kotroni, V., Lagouvardos, K.,
972 Varinou, M., Papadopoulos, A., and Luria, M.: Some Observational and Modelling Evidence of
973 Long Range Transport of Air Pollutants from Europe Towards the Israeli Coast, J. Geophys.
974 Res., 105, 7177-7186, 2000.
975 Worden, J., Kulawik, S., Frankenberg, C., Payne, V., Bowman, K., Cady-Peirara, K., Wecht, K.,
976 Lee, J. E., and Noone, D.: Profiles of CH4, HDO, H2O, and N2O with improved lower

977 tropospheric vertical resolution from Aura TES radiances, Atmos. Meas. Tech., 5, 397–411,
978 www.atmos-meas-tech.net/5/397/2012/doi:10.5194/amt-5-397-2012, 2012.
979 Wunch, D., Toon, G. C., Wennberg, P. O., Wofsy, S. C., Stephens, B. B., Fischer, M. L., Uchino,
980 O., Abshire, J. B., Bernath, P., Biraud, S. C., Blavier, J.-F. L., Boone, C., Bowman, K. P.,
981 Browell, E. V., Campos, T., Connor, B. J., Daube, B. C., Deutscher, N. M., Diao, M., Elkins, J.
982 W., Gerbig, C., Gottlieb, E., Griffith, D. W. T., Hurst, D. F., Jiménez, R., Keppel-Aleks, G.,
983 Kort, E. A., Macatangay, R., Machida, T., Matsueda, H., Moore, F., Morino, I., Park, S.,
984 Robinson, J., Roehl, C. M., Sawa, Y., Sherlock, V., Sweeney, C., Tanaka, T., and Zondlo, M. A.:
985 Calibration of the Total Carbon Column Observing Network using aircraft profile data, Atmos.
986 Meas. Tech., 3, 1351-1362, doi:10.5194/amt-3-1351-2010, 2010.
987 Xiong, X., Barnet, C., Maddy, E., Sweeney, C., Liu, X., Zhou, L., and Goldberg, M.:
988 Characterization and validation of methane products from the Atmospheric Infrared Sounder
989 (AIRS), J. Geophys. Res., 113, G00A01, doi:10.1029/2007JG000500., 2008.
990 Yokota, T., Yoshida, Y., Eguchi, N., Ota, Y., Tanaka, T., Watanabe, H., and Maksyutov, S.: Global
991 Concentrations of CO2 and CH4 Retrieved from GOSAT: First Preliminary Results, SOLA, 5,
992 160-163, doi:10.2151/sola.2009, 2009.
993 Yoshida, Y., Kikuchi, N., Morino, I., Uchino, O., Oshchepkov, S., Bril, A., Saeki, T., Schutgens,
994 N., Toon, G. C., Wunch, D., Roehl, C. M., Wennberg, P. O., Griffith, D. W. T., Deutscher, N.
995 M., Warneke, T., Notholt, J., Robinson, J., Sherlock, V., Connor, B., Rettinger, M., Sussmann,
996 R., Ahonen, P., Heikkinen, P., Kyrö, E., Mendonca, J., Strong, K., Hase, F., Dohe, S., and
997 Yokota, T.: Improvement of the retrieval algorithm for GOSAT SWIR XCO2 and XCH4 and
998 their validation using TCCON data, Atmos. Meas. Tech., 6, 1533-1547, doi:10.5194/amt-6-
999 1533-2013, 2013.
1000 Ziv, B., Saaroni, H., and Alpert, P.: The factors governing the summer regime of the eastern
1001 Mediterranean, Int. J. Climatol., 24, 1859–1871, doi: 10.1002/joc.1113, 2004.
1002

1002 **Table 1.** Nadir-viewing instruments having the capabilities to measure CH_4 in the troposphere.
1003 Please, refer to the text for the acronyms.
1004

Platform	**Instrument**	**Operation time**	**Wavelength**	**References**
ADEOS-1	IMG	1996-1997	TIR	Clerbaux et al. (1998)
ENVISAT	SCIAMACHY	2002-2012	NIR	Buchwitz et al. (2000)
Aura	TES	2004-date	TIR	Worden et al. (2012)
GOSAT	TANSO-FTS	2008-date	SWIR & TIR	Yokoto et al. (2009)
Aqua	AIRS	2004-date	TIR	Xiong et al. (2008)
MetOp-A	IASI	2008-date	TIR	Hilton et al. (2012)
MetOp-B	IASI	2012-date	TIR	
MetOp-C	IASI	Expected in 2016	TIR	

1005
1006
1007

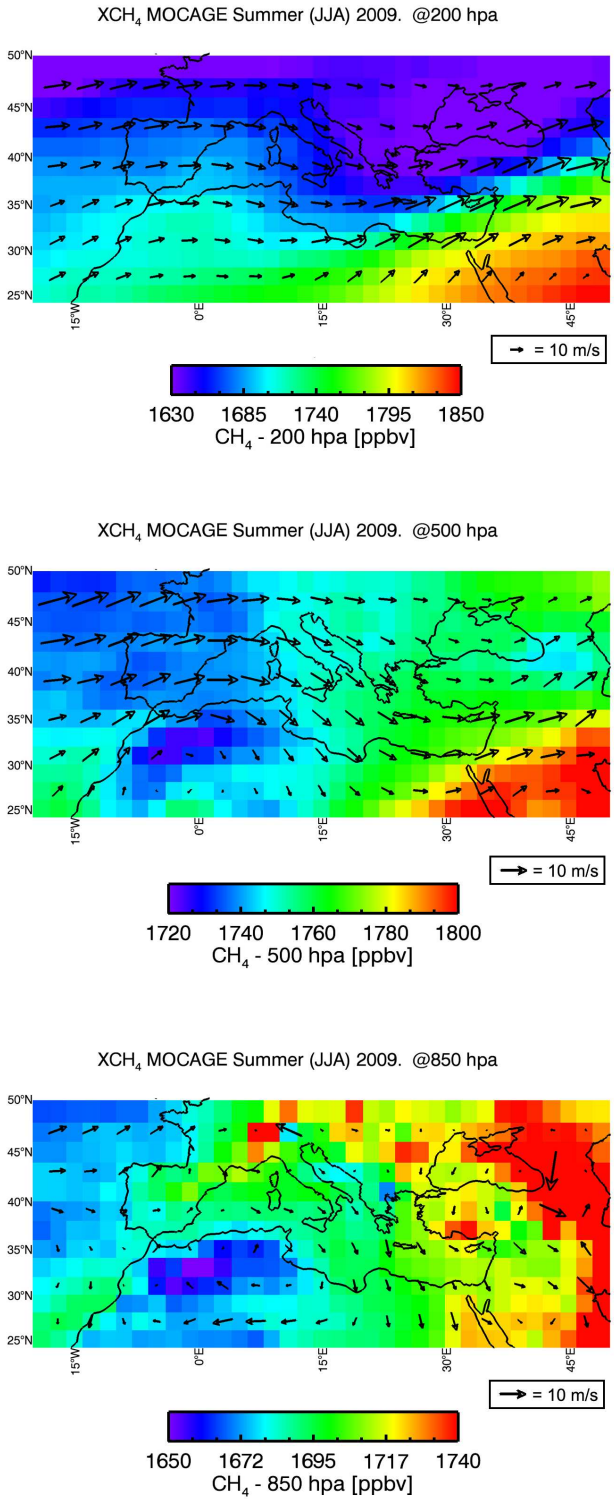

1007

1008 **Figure 1.** (From bottom to top) Fields of CH_4 as calculated by MOCAGE and averaged for summer
1009 (JJA) 2009 at 850, 500 and 200 hPa. Superimposed are the horizontal winds from ARPEGE
1010 averaged over the same period. In order to highlight the CH_4 horizontal gradients, the range of the
1011 colour scale changes from top to bottom.

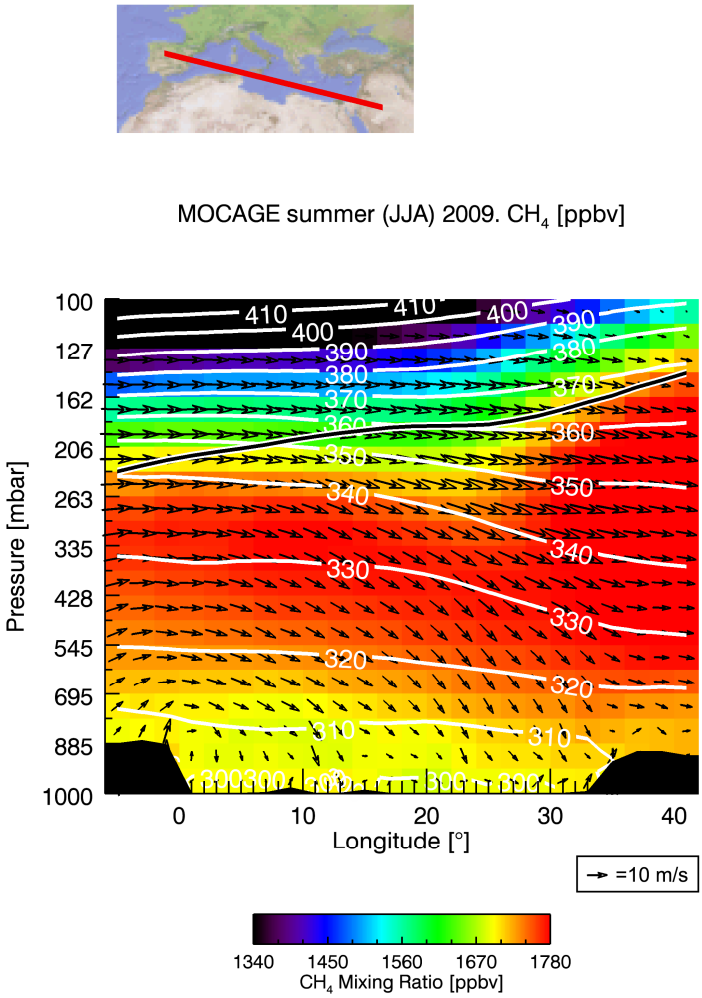

Figure 2. Vertical distribution of CH_4 as calculated by MOCAGE and averaged for JJA 2009 as a function of longitude along the red line represented above the Figure. Superimposed are the associated longitudinal and vertical winds from ARPEGE, together with the isentropes (white lines) and the cold point tropopause from NCEP/NCAR reanalyses (black line) averaged over the same period.

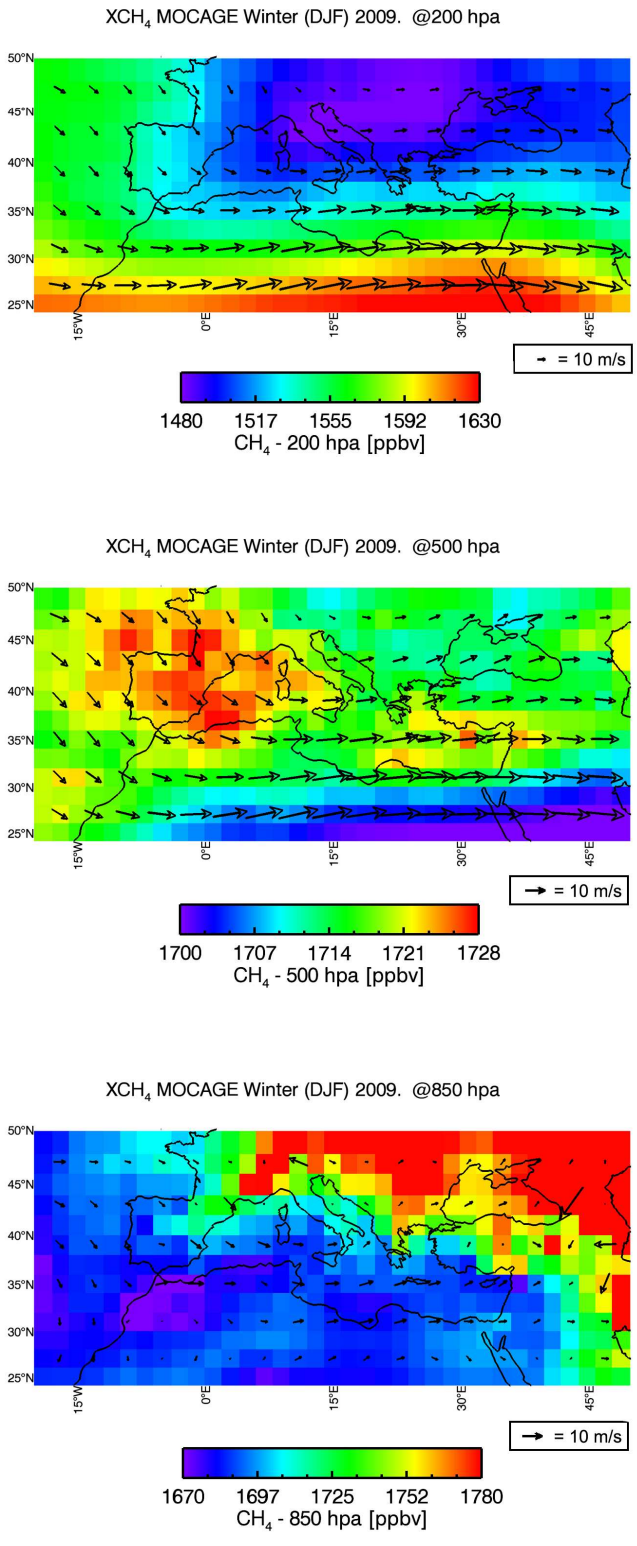

1020

1021 **Figure 3.** Same as Fig. 1, but for winter (DJF) 2009.

1022

1023

1023

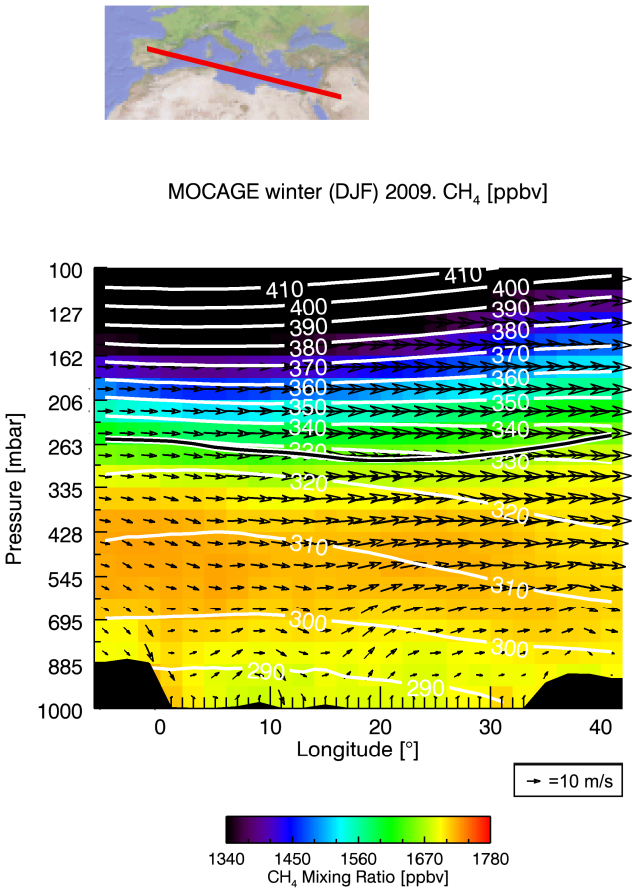

1024

1025 **Figure 4.** Same as Fig. 2, but for winter (DJF) 2009.

1026

1027

1027

1028

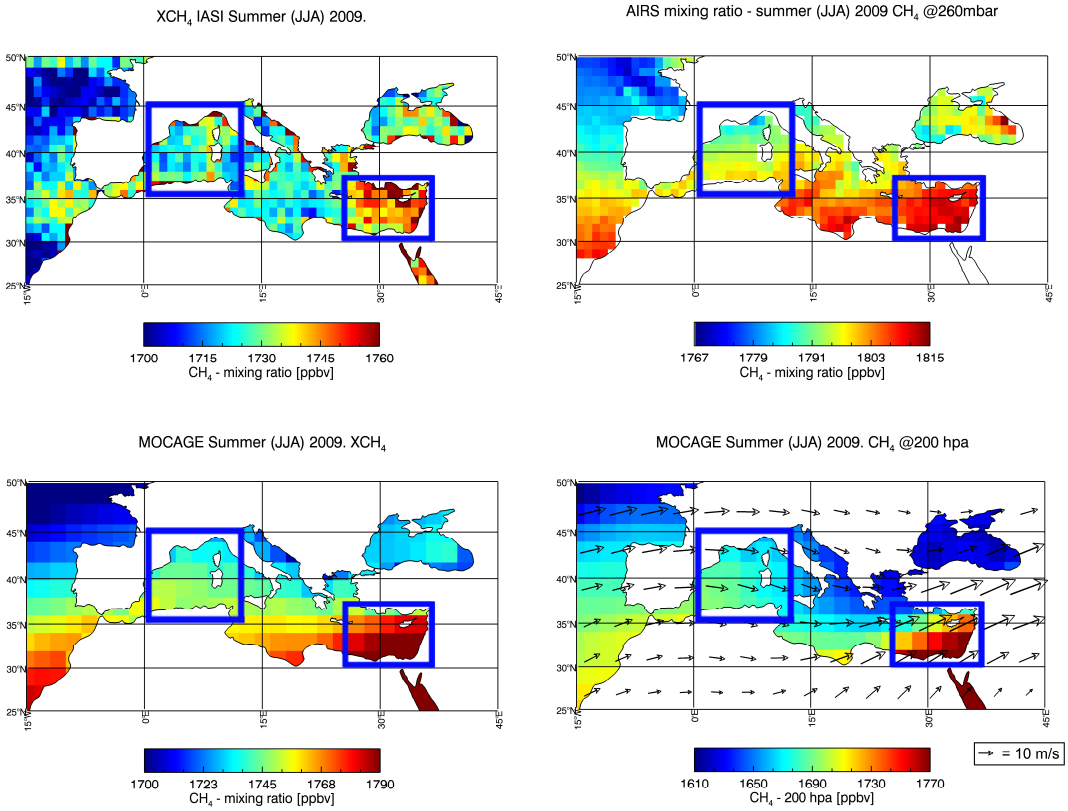

1029

1030 **Figure 5.** Field of total columns of CH_4 as measured by IASI and averaged for summer (JJA) 2009
1031 (top left), and field of CH_4 at 260 hPa as measured by AIRS and averaged for JJA 2009 (top right).
1032 (Bottom) Same as above but as calculated by MOCAGE. Satellite data are represented in a 1°x1°
1033 resolution whilst model data are shown in a 2°x2° resolution. The two blue squares in the lower left
1034 Figure represent the Western and Eastern Mediterranean Basins where the measured and modelled
1035 data are selected over the Mediterranean Sea. Superimposed are the horizontal winds from
1036 ARPEGE at 200 hPa averaged over the same period (bottom right). In order to highlight the CH_4
1037 horizontal gradients, the range of the colour scale changes for each figure.

1038

1039

1039

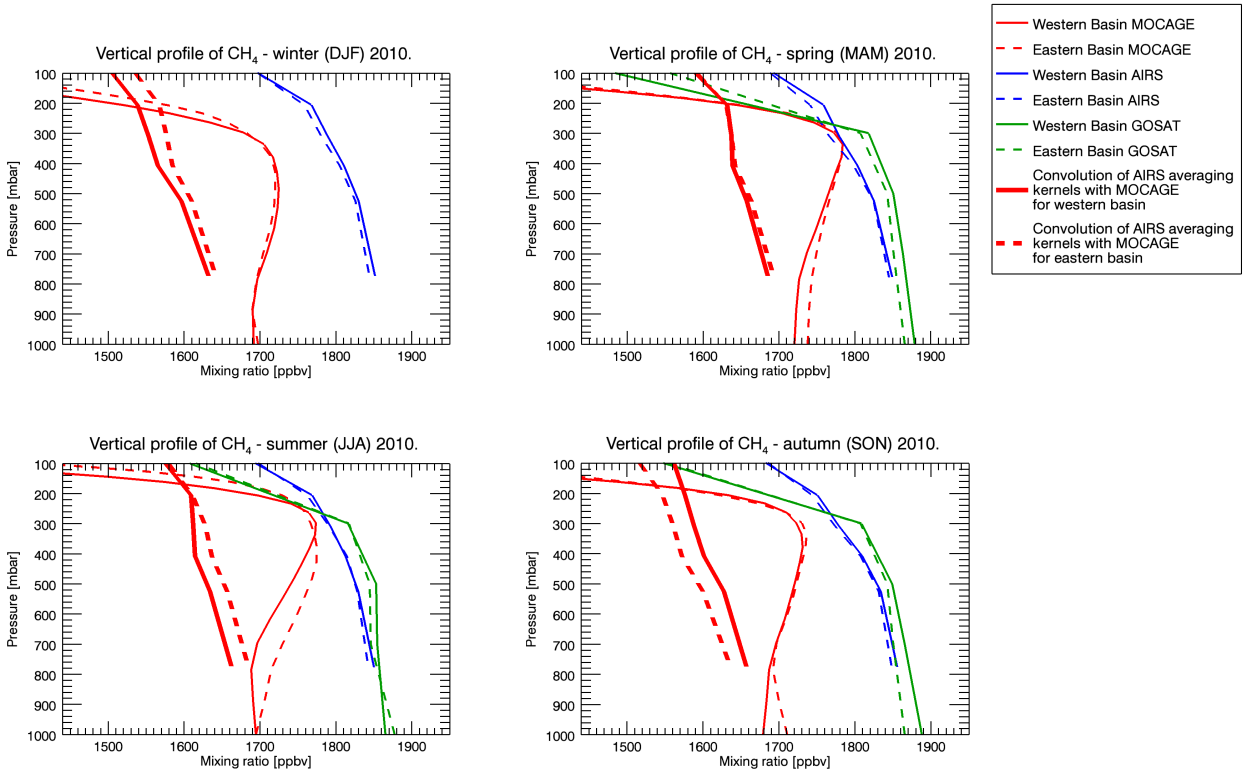

1040

1041 **Figure 6.** (From top to bottom and from left to right) Seasonally-averaged vertical profiles of CH_4
1042 as measured by AIRS (blue lines) and GOSAT (green lines), and as calculated by MOCAGE (thin
1043 red lines) over the Eastern (dashed lines) and Western (solid lines) MBs in winter, summer, spring
1044 and autumn 2010. Also shown are the seasonally-averaged MOCAGE profiles convolved with the
1045 AIRS averaging kernels (thick red lines) for the four seasons over the Eastern (dashed lines) and
1046 Western (solid lines) MBs.

1047

1048

1048

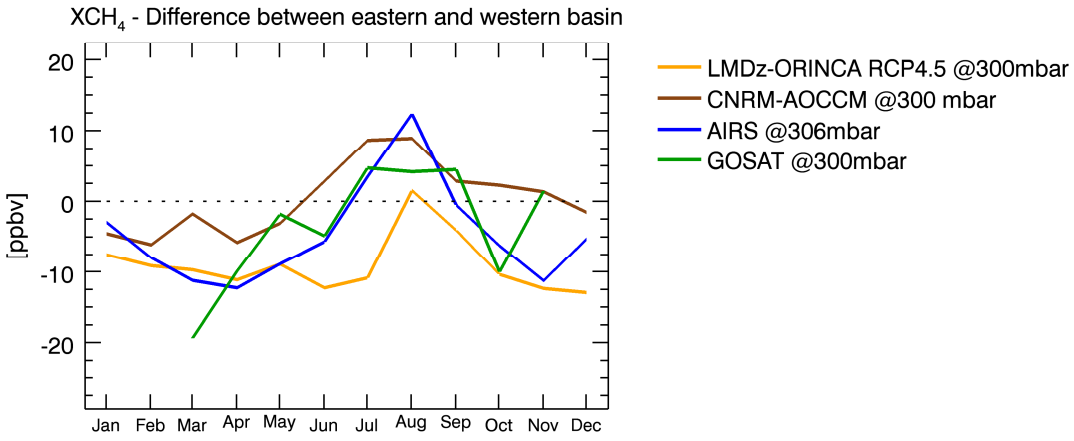

1049

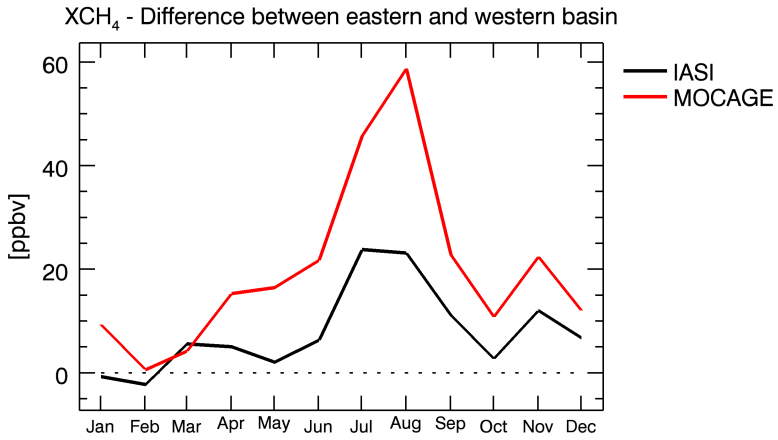

1050

1051 **Figure 7.** (Top) Seasonal evolution of the difference in the CH_4 fields between the Eastern and
1052 Western MB as measured by AIRS (blue line) and GOSAT (green line) at 306 and 300 hPa,
1053 respectively and as calculated by LMDz-OR-INCA (yellow line) and CNRM-AOCCM (brown
1054 line). (Bottom) Seasonal evolution of the difference in the CH_4 total columns between the Eastern
1055 and Western MB as measured by IASI (black line) and as calculated by MOCAGE (red line). The
1056 LMDz-OR-INCA and CNRM-AOCCM data sets cover the climatological period 2001-2010. The
1057 MOCAGE and IASI data sets cover the period 2008-2011 whilst the satellite AIRS and GOSAT
1058 data sets are representative of the year 2010.

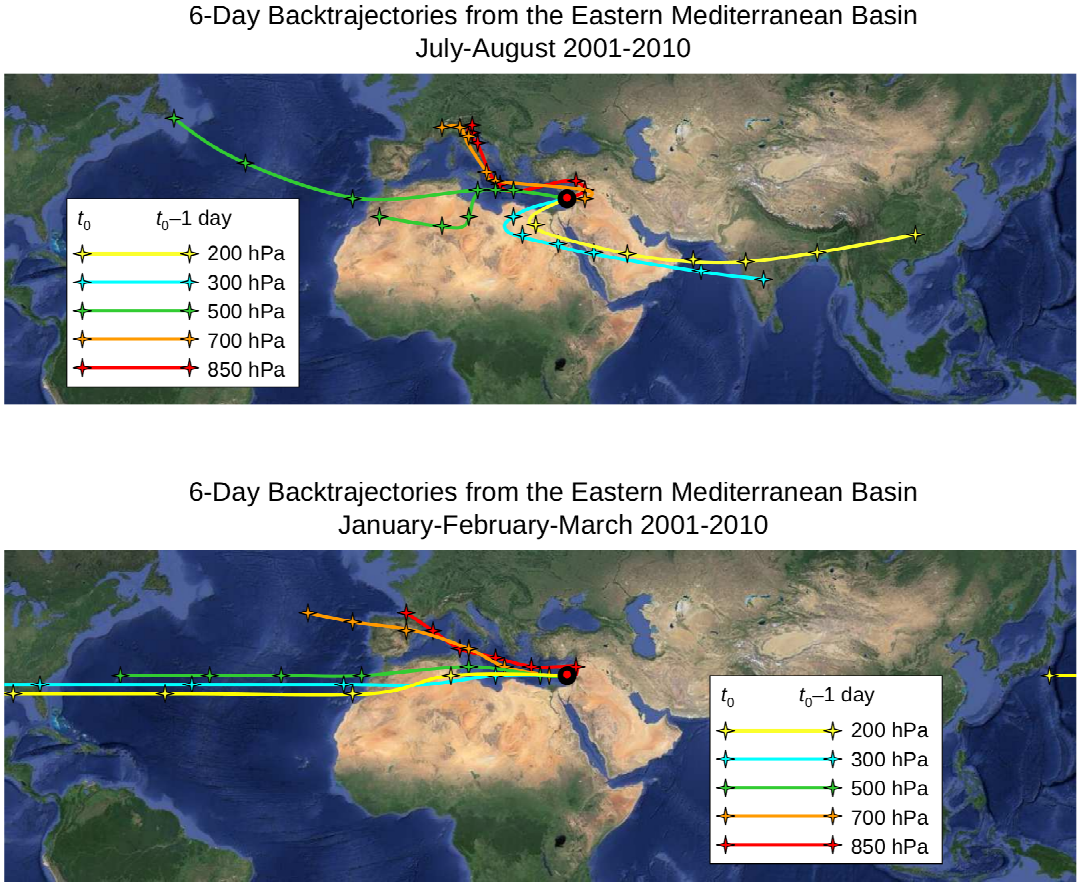

Figure 8. (Top) Climatological six-day back-trajectories from the point at 33° N, 35° E located in the Eastern Mediterranean Basin (red filled circle) calculated from the British Atmospheric Data Centre trajectory service (http://badc.nerc.ac.uk/community/trajectory/) from 1st July to 31st August from 2001 to 2010 every 12 hours at 850 (red line), 700 (orange line), 500 (green line), 300 (blue line) and 200 hPa (yellow line). The position of the gravity center of each distribution at each level is represented every 24 hours by a star. (Bottom) Same as top, but calculated from 1st January to 31st March 2001-2010.

1068

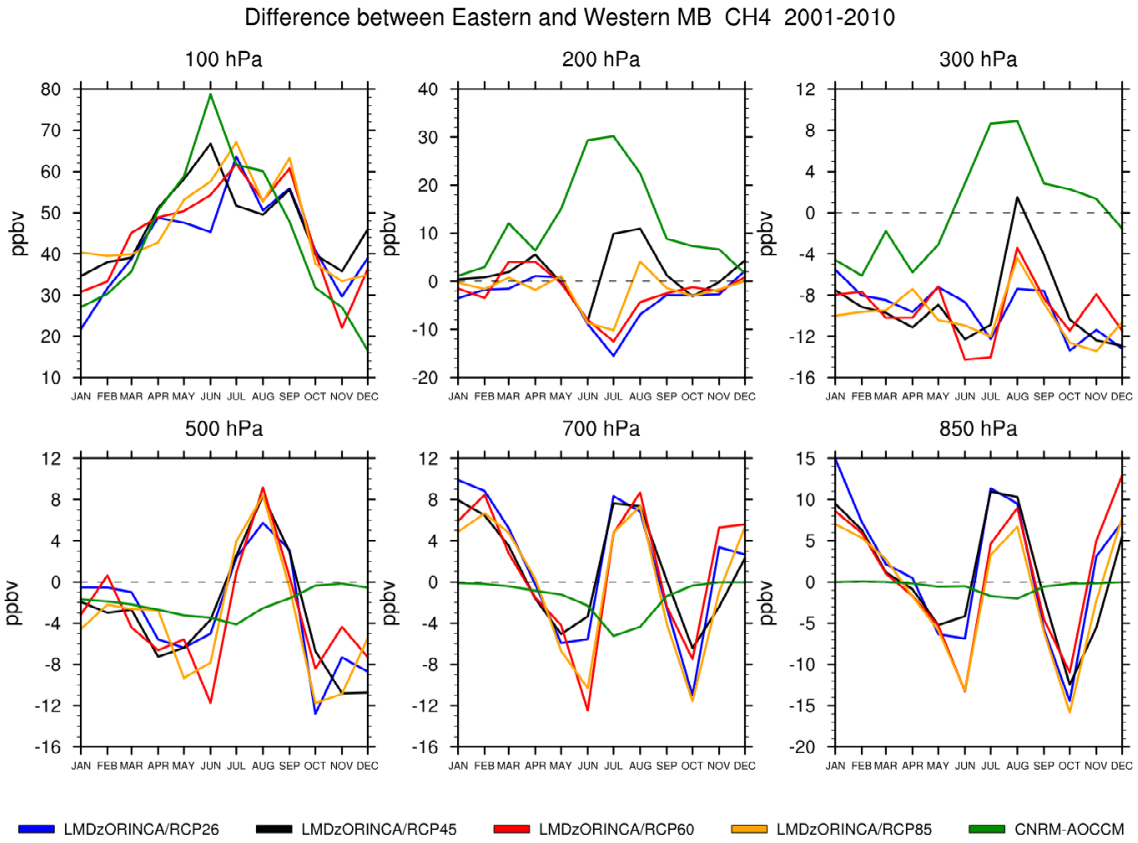

1069

1070 **Figure 9.** (From top to bottom and from left to right) Seasonal evolution of the difference in the
1071 CH_4 fields between the Eastern and Western MB over the climatological period 2001-2010 at 100,
1072 200, 300, 500, 700 and 850 hPa as calculated by CNRM-AOCCM (green) model and LMDz-OR-
1073 INCA according to the 4 IPCC scenarios: RPCs 2.6 (blue), 4.5 (black), 6.0 (red) and 8.5 (yellow).
1074 See section 2.2 for more details.

1075

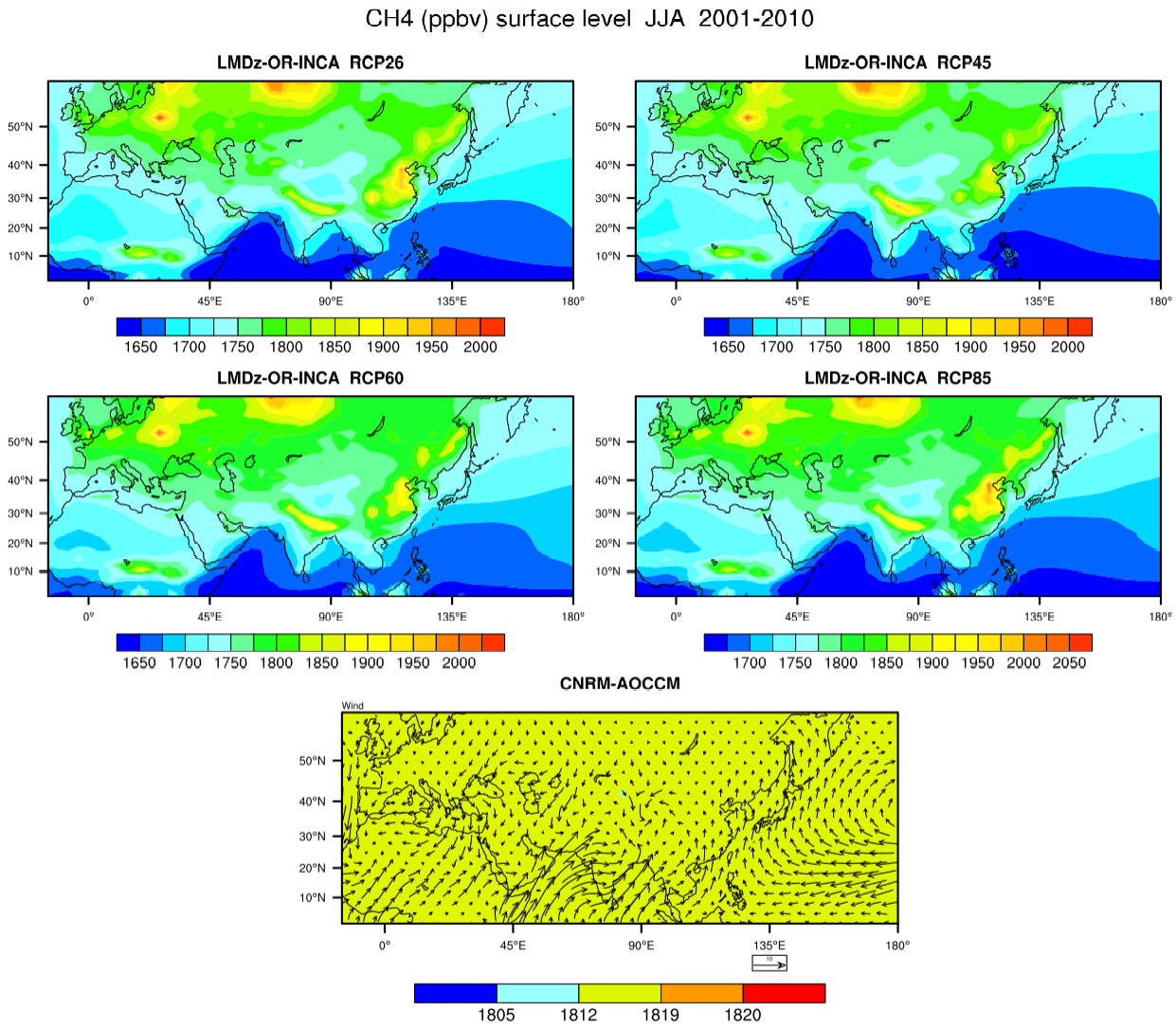

1076

1077 **Figure 10.** Fields of surface CH_4 as calculated by the CNRM-AOCCM model (bottom) and the
1078 LMDz-OR-INCA model (top and centre) according to the 4 IPCC scenarios (RCPs 2.6 (top left),
1079 4.5 (top right), 6.0 (centre left) and 8.5 (centre right)) averaged over the summer season (JJA) and
1080 the climatological period 2001-2010. Superimposed to the CNRM-AOCCM CH_4 fields (bottom) is
1081 the wind field at the surface averaged over the same period. Note that the range of the colour scale
1082 changes for each figure and that the surface CH_4 for CNRM-AOCCM (bottom) is constant.

1083

1084

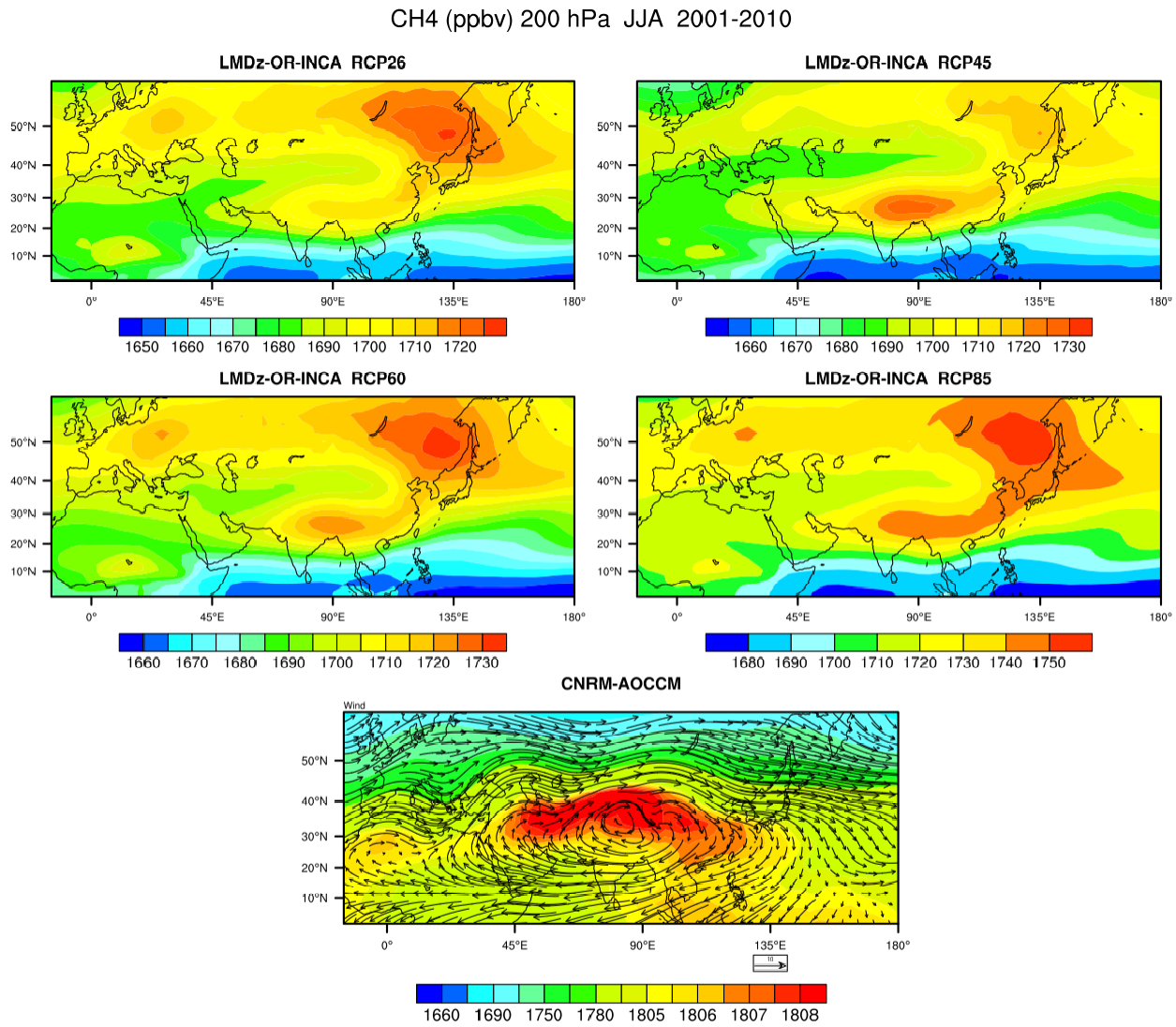

1084

1085 **Figure 11.** Fields of CH_4 as calculated by the CNRM-AOCCM model (bottom) and the LMDz-OR-
1086 INCA model (top and centre) considering the 4 IPCC scenarios (RCPs 2.6 (top left), 4.5 (top right),
1087 6.0 (centre left) and 8.5 (centre right)) at 200 hPa averaged over the summer season (JJA) and the
1088 climatological period 2001-2010. Superimposed to the CNRM-AOCCM CH_4 fields (bottom) is the
1089 wind field at 200 hPa averaged over the same period. Note that the range of the colour scale
1090 changes for each figure and that the colour scale for the CNRM-AOCCM model (bottom) is non
1091 linear.

1092

1093

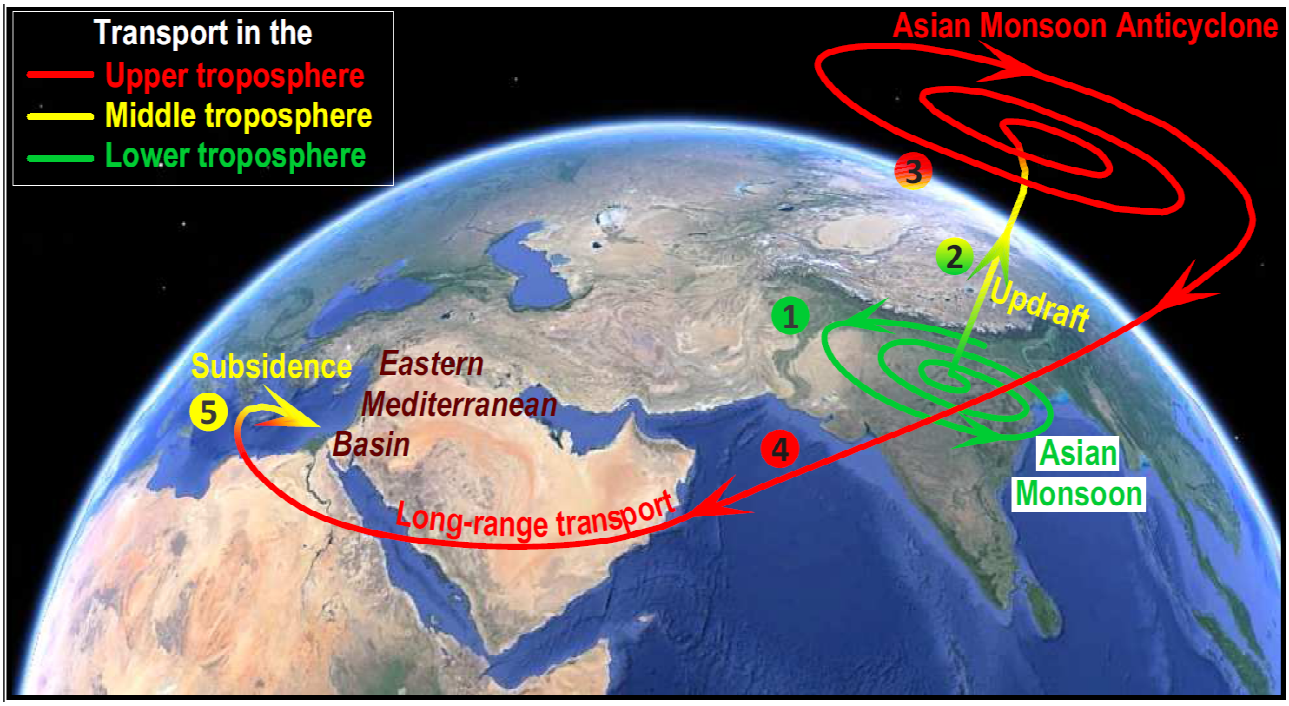

Figure 12. Schematic representation of the processes impacting the mid-to-upper tropospheric pollutants, including CH_4, above the Eastern Mediterranean Basin in summer (July-August). (1) Trapping of lower tropospheric pollutants in the Asian monsoon. (2) Updraft of pollutants in the Asian monsoon up to the upper troposphere. (3) Build-up of pollutants within the Asian monsoon in the upper troposphere. (4) Large-scale re-distribution of pollutants by the Asian Monsoon Anticyclone to the Middle East and North Africa in the upper troposphere. (5) Build-up of pollutants though descent down to the middle troposphere above the Eastern Mediterranean Basin.